

PIRAEUS UNIVERSITY OF APPLIED SCIENCES

Zoi Georgakopoulou

Aerodynamic Analysis of Rotor 37 using CFD

SCHOOL OF TECHNOLOGICAL APPLICATIONS

Mechanical Engineering

Ptychion

Academic Year: 2015 - 2016

Supervisor: Professor Pericles Pilidis

Academic Advisor: Dr. Konstantinos-
Stefanos Nikas

December 2015

ABSTRACT

Turbomachinery blades are required to perform reliably and efficiently over a variety of operational conditions and thus their shape has been studied extensively and is highly optimised. The development of turbomachinery manufacturing lies largely on CFD simulations that are followed by validation through experimental data. That way, costs are reduced, while experiments are limited and already optimised and manufacturing is optimised. As a result, more efficient components and therefore more efficient engines are created. In this thesis, a 3-D CFD analysis of a datum fan was conducted and the results were validated against experimental data in order to study and assess the aerodynamic behaviour of the component.

Keywords:

CFD, Rotor 37, Aerodynamic Analysis, Validation

ACKNOWLEDGEMENTS

My bachelor thesis project has been a long and tough journey with many ups and downs, but it is finally complete. First and foremost, I would like to thank Dr Konstantinos-Stefanos Nikas who has been supportive and patient for that long. I can never pay you back for what you have done for me. I would also like to thank the Erasmus Office of Piraeus University of Applied Sciences for their help, support and patience. During my studies, many people have inspired me into different engineering principles; Dr Alexis, Dr Sideris, Dr Moustris, Mr Zafirakis and Professor Kaldellis.

In the Cranfield world, I would like to thank Professor Pilidis for the opportunity he gave me and the trust he has shown to me. He has been a great source of inspiration in many levels. Also, Thanos Kiatipis and Spyros Kontogiannis were my first family here and have a great space in my heart.

My big, greek family: -Mum, Dad, Panagiotis, Giannis, Nikos, Stefanos- Giagia Christina and Giagia Eirini; I love you unconditionally and miss you more every day. Madame Roula and Elina Vervessou are sources of inspiration for different reasons, as well as Stella Kontaxaki. You're in my heart.

Losing your everyday life with your real friends has an impact in one's life. Nancy, Vanessa, Nansy, Maria, Aggeliki, I miss the way we communicate. Connection that deep is kind of irreplaceable. I love you all and always!

Finally, the two people that have really been my support system are Aggeliki Kalpaxoglou and Olivier Bouzigues. I am grateful to you both for your different levels of support. Aggeliki, I love you, you're always there and I'm trying to always be there too! I miss you and I don't miss you. Because we'll grow old together no matter what! Ramoto, thank you for taking care of me. I'm grateful for everything

Zoi Georgakopoulou

December 2015

TABLE OF CONTENTS

ABSTRACT	2
ACKNOWLEDGEMENTS.....	3
LIST OF FIGURES.....	5
LIST OF TABLES	8
LIST OF ABBREVIATIONS	9
1 INTRODUCTION	12
1.1 Project objectives.....	12
1.2 Thesis layout and structure.....	13
2 AXIAL FLOW COMPRESSOR AERODYNAMIC DESIGN.....	14
2.1 Theoretical background.....	14
2.1.1 Introduction to axial compressors.....	14
2.1.2 Elementary theory	15
2.1.3 Parameters affecting the pressure ratio	20
2.1.4 Blockage factor.....	22
2.1.5 Annulus configuration.....	23
2.2 Design Process.....	25
2.2.1 Preliminary Design	26
2.2.2 Through Flow Design	27
2.2.3 Blade to Blade Design.....	28
2.2.4 Three Dimensional Analysis	29
2.3 Blade Geometry	29
2.3.1 Incidence angle	31
2.3.2 Deviation angle.....	32
2.4 Axial flow compressor blade profile families.....	32
2.4.1 NACA 65-Series	33
2.4.2 British C-series	33
2.4.3 Double Circular Arc	33
2.4.4 Multiple Circular Arc	35
2.5 Rotor 37	35
Test case details	35
3 3D MODEL GENERATION FOR CFD ANALYSIS.....	38
3.1 Introduction	38
3.2 The CFD modelling process.....	39
3.3 Defining the 3D Geometry	40
3.4 Grid Generation	43
3.4.1 Grid quality assessment.....	45
3.5 Set up of the CFD simulation	48
3.5.1 Specification of the boundary and initial conditions.....	48
4.6 Turbulence model	50
4.7 Grid dependency study	51

4.8	Monitoring the CFD simulation.....	52
5	CFD results and discussion	54
5.1	Baseline geometry	54
5.1.1	Model Validation.....	54
5.1.2	Verification of the mesh clustering.....	57
5.1.3	Rotor 37 characteristic	58
5.1.4	Flow details	60
6	CONCLUSIONS ANDRECOMMENDATIONS	67
6.1	Conclusions	67
6.2	Recommendations for further work	68

LIST OF FIGURES

Figure 1: Compressor stage and T-s diagram (3).....	15
Figure 2: Single stage velocity triangle (7)	16
Figure 3: Combined velocity triangles (5)	19
Figure 4: Blade spacing and velocity distribution through passage (3)	22
Figure 5: Blockage factor annulus correction (5).....	23
Figure 6: Typical compressor annulus diagram (10)	24
Figure 7: Compressor annulus configurations (10).....	24
Figure 8: Typical gas turbine design procedure	26
Figure 9: Blade meridional plane (13)	28
Figure 10: Cascade nomenclature (3).....	30
Figure 11: Deflection and Loss coefficient against air inlet angle (9)	31
Figure 12: DCA typical profile (13).....	34
Figure 13: Pressure distribution comparison (13)	35
Figure 14: Rotor 37 measurement stations (22)	36
Figure 15: ANSYS Workbench Project Schematic.....	39
Figure 16: Simulation procedure.....	40
Figure 17: BladeGen GUI	41
Figure 18: NASA Rotor 37 hub geometry file (23)	41
Figure 19: Mesh statistics.....	46
Figure 20: Observing the midspan Leading Edge O-Grid	46
Figure 21: Meshed domain.....	47
Figure 22: Blade domain definition	50
Figure 23: Grid sensitivity analysis.....	52
Figure 24: Momentum, Mass and Efficiency residuals of a converging solution.....	53
Figure 25: Published Efficiency results of Rotor 37 (22)	54
Figure 26: Published PR and TR results of Rotor 37 (Dunham, 1988)	55
Figure 27: Rotor 37 experimental and computed Efficiency	56
Figure 28: Rotor 37 experimental and computed Pressure Ratio.....	56
Figure 29: Rotor 37 experimental and computed Temperature ratio	56
Figure 30: Axial distribution of y^+ along the blade midspan	58
Figure 31: Overall Pressure Ratio against Normalized Mass Flow	59
Figure 32: Overall Efficiency over Normalised Mass Flow	59
Figure 33: Baseline Mach number contour at 5% span	61
Figure 34: Baseline Mach number contour at 50% span	61
Figure 35: Baseline Mach number contour at 90% span	62
Figure 36: Baseline blade loading chart at 5% span	63
Figure 37: Baseline blade loading chart at 50% span	63
Figure 38: Baseline blade loading chart at 90% span	64
Figure 39: Baseline streamlines on suction side	64
Figure 40: Baseline hub to shroud efficiency distribution	65
Figure 41: Baseline hub to shroud total pressure distribution.....	66
Figure 42: Baseline hub to shroud total temperature distribution.....	66

LIST OF TABLES

Table 1: Typical values of blockage factor (5).....	23
Table 2: Rotor 37 inlet boundary conditions (22)	36
Table 3: Basic aerodynamic design parameters	37
Table 4: Grid sensitivity study cases	51
Table 5: Simulation results for different back pressures	58

LIST OF ABBREVIATIONS

AGARD	Advisory Group for Aerospace Research & Development
BPR	By-Pass Ratio
c	Chord
CFD	Computational Fluid Dynamics
C_p	Specific heat capacity at constant pressure
CPR	Compressor Pressure Ratio
DCA	Double Circular Arc
DF	NACA Diffusion Factor
DF	Diffusion Factor
dH	De Haller Number
ERCOFTAC	European Research Community On Flow, Turbulence and Combustion
FOD	Foreign Object Damage
FPR	Fan Pressure Ratio
GUI	Graphic User Interface
HPC	High Pressure Compressor
HPT	High Pressure Turbine
IGTI	International Gas Turbine Institute
IGV	Inlet Guide Vanes
ISA	International Standard Atmosphere
ITP	Industria des Turbo Propulsores
LDA	Laser Doppler Anemometry
LE	Leading Edge
LPC	Low Pressure Compressor
MCA	Multiple Circular Arc
NACA	National Advisory Committee for Aeronautics
NASA	National Aeronautics and Space Administration
NDMF	Non Dimensional Mass Flow
OPR	Overall Pressure Ratio
PS	Pressure Side
RANS	Reynolds Averaged Navier Stokes
Re	Reynolds

RMS	Root Mean Square
s	Pitch
SCM	Streamline Curvature Method
SFC	Specific Fuel Consumption
SLS	Sea Level Standard
SS	Suction Side
SST	Shear Stress Transport
TE	Trailing Edge
η	Efficiency
ρ	Density
ϕ	Flow Coefficient
ψ	Loading Coefficient

1 INTRODUCTION

Turbomachinery blades are required to perform reliably and efficiently over a variety of operational conditions and thus their shape has been studied extensively and is highly optimised. Although manufacturing techniques have advanced notably (electro-chemical machining, flank milling, etc), finished blades deviate inevitably from their design intent. Noisy industrial processes from shaping the desired component to surface finishing, assembling inaccuracy, mechanical failure models such as LE erosion or corrosion, FOD and ingestion of particulates that occur during the engine operation, all introduce geometric uncertainty (1).

It is generally accepted that geometric variability is not desirable in turbomachinery components. However little is known in detail regarding the impact of geometric uncertainty on gas turbine components. The following comparison helps to better understand the impact of this geometric uncertainty. Roberts reports that core compressor blade LE erosion results in more than 3% increase on thrust specific fuel consumption. It is worth noting that a 1% change in fuel burn may lead a fleet operator to profitability or loss (2).

This work aims to investigate the flow characteristics of a transonic fan using CFD tools. A high fidelity CFD model, able to resolve to length scales similar to the microscopic geometric errors that need to be assessed and the results were validated through experimental results.

1.1 Project objectives

This project's main goal is to study the aerodynamic performance of rotor 37 in 3D using CFD tools. Rotor 37 was chosen as it is a very well documented case from NASA and literature can provide the author with accurate validation data. In that way, the author familiarised herself with turbomachinery, gas turbines' technology and most importantly, CFD tools and methods on how to complete and validate a robust simulation.

To meet this objective, the steps that were undertaken include:

- Creation of a high fidelity CFD model on the basis of the above design
- 3D passage flow analysis using CFD post-processing tools
- Investigation of the flow characteristics

1.2 Thesis layout and structure

This thesis consists of three main parts. The choice of the baseline geometry, the creation of a 3D CFD model based on the baseline geometry and the analysis of the CFD results.

Chapter 2 provides the theoretical background for conducting a preliminary design of an axial compressor and the reason why rotor 37 was chosen to be the examined case.

Chapter 3 discusses the fundamentals of computational fluid dynamics.

Chapter 4 is dedicated to the CFD model creation and describes the implementation of the geometry in the CFD software, the generation the mesh and how the simulation was prepared.

Chapter 5 presents and compares the CFD results with the experimental work.

Finally, Chapter 6 discusses the conclusions drawn by the analysis and recommendations for future work were presented.

2 AXIAL FLOW COMPRESSOR AERODYNAMIC DESIGN

2.1 Theoretical background

2.1.1 Introduction to axial compressors

The majority of civil and military aircraft are nowadays powered by gas turbine engines, also known as jet engines. The basic idea of the turbojet engine is simple and, for a modern gas turbine engine that is at the forefront of technology, can be described as following. Air taken in from an opening in the front of the engine is compressed as much as 45 times. Fuel is then added and the air is burned in order to raise the temperature of the fluid mixture to more than 1800 K (3). The resulting hot gases expand and form a fast moving jet which generates the thrust required to move the aircraft as stated by Newton's second law of motion. Although in practice there exist several different configurations of gas turbines according to their application, they all work under the same principles and as such their core is the same and they share some fundamental parts. Thus, all gas turbines have a compressor whose function is to increase the incoming air pressure before it enters the combustion chamber and can be found in two different main types: axial and centrifugal (4). Early on in the history of gas turbines engines, axial flow compressors were identified with both higher pressure ratio – necessary for reducing specific fuel consumption - and higher efficiency than the centrifugal ones. Axial compressors offer also another major advantage allowing a much larger flow rate for a given frontal area. As a result, the axial flow machines dominate the field for jet engines and large power stations restricting the centrifugal compressors only to the applications where the flow is really small and cannot be handled efficiently with axial blading (3).

In axial flow compressors, the working fluid enters the engine parallel to the axis of rotation and passing through the compressor stages it exits the component at the designed exit angle and at a higher pressure and temperature. Each stage consists of a rotor and a stator. The flow experiences initially an increase in its kinetic energy by accelerating through the rotating airfoils or blades of the rotor, which is subsequently diffused at stationary airfoils or vanes of the stator and turned into pressure (5).

- Newton's second law
- Conservation of mass

For the rest of this report any reference to the above four laws will make use of their engineering titles, namely:

- The conservation of energy
- The concept of entropy
- The conservation of momentum
- The mass flow continuity

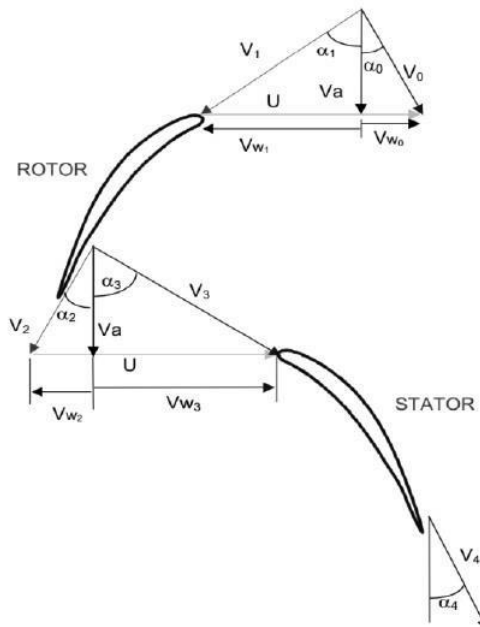


Figure 2: Single stage velocity triangle (7)

Considering the simple case of a flow in a gas turbine compressor inlet, the total specific (i.e. per unit mass) energy of the flow can be quantified in terms of specific enthalpy, $C_p t$, and specific kinetic energy, $V^2/2$.

Therefore, using the notation of Figure 2 above, the total energy at the stage inlet is:

$$C_p T_0 = C_p t_0 + \frac{V_0^2}{2}$$

At the stage outlet, the total energy is:

$$C_p T_4 = C_p t_4 + \frac{V_4^2}{2}$$

Assuming no energy is exchanged across the compressor stage with the surroundings (adiabatic process):

$$C_p T_3 = C_p T_4$$

The change of total specific energy across the stage, also known as stagnation enthalpy is therefore:

$$C_p(T_3 - T_0) = C_p \Delta T = \Delta H$$

Where C_p is the specific heat, V_0 and V_4 are the rotor inlet and stator outlet absolute velocities respectively, T_0 , T_3 and T_4 are the stagnation temperatures at rotor inlet, stator inlet and stator outlet respectively, ΔT is the change in total temperature and ΔH the change in total energy.

Taking into consideration the rate of change in angular momentum of the working fluid in the direction of rotation and referring to it as the Torque, T , this is described by:

$$T = \frac{\delta m(r_2 V_{w3} - r_1 V_{w0})}{\delta t}$$

Where V_{w0} is the whirl component of the rotor inlet absolute velocity or inlet whirl, and V_{w3} the outlet whirl.

According to the conservation of energy the work done per unit mass flow must equal to the total specific energy across the stage. Noting that the work rate and the blade peripheral speed equal to $W=T\omega$ and $U=\omega r$ respectively, a combination of the above equations leads to the following expression, which is a fundamental equation for turbomachinery problems and is better known as the Euler's turbine equation (7):

$$C_p \Delta T = \Delta H = U_2 V_{w3} - U_1 V_{w0}$$

Where U_1 and U_2 are the blade peripheral speeds at the inlet and the outlet of the rotor respectively.

Assuming that the mean radius remains constant the above equations becomes

$$\Delta H = U(V_{w3} - V_{w0}) = U \Delta V_w$$

Considering now that the axial velocity, V_a , also remain constant along the rotor, two basic trigonometry equations can be readily seen from the geometry of the velocity triangles of Figure 2.

$$\frac{U}{V_a} = \tan a_0 + \tan a_1$$

$$\frac{U}{V_a} = \tan a_2 + \tan a_3$$

The inlet and outlet whirl in Euler's turbine equation can be then put in terms of axial velocity and air angles to give:

$$\Delta H = UV_\alpha(\tan a_3 - \tan a_0) = UV_\alpha(\tan a_1 - \tan a_2)$$

This energy input is absorbed in order to raise the working fluid pressure and overcome any losses taking place in the procedure and reveals itself as a total temperature rise, ΔT . Equating (4.6) and (4.9), the stage total temperature rise is equal to:

$$\Delta H = \frac{UV_\alpha}{C_p}(\tan a_1 - \tan a_2)$$

Assuming that during the compression process no heat is exchanged with the surroundings (i.e. isentropic), we can create a “platform” against which the actual performance of the compressor can be compared. In this ideal state the pressure of the fluid is proportional to its temperature according to the following relationship: $p \propto T^{\frac{\gamma}{\gamma-1}}$

And thus the compressor overall pressure ratio is given by the expression:

$$\text{OPR} = \frac{P_2}{P_1} = \frac{T_2^{\frac{\gamma}{\gamma-1}}}{T_1}$$

The efficiency of the compression, η_{is} , is an engineering term used to take into consideration the losses that are present in the real stage and is defined as:

$$\eta_{is} = \frac{\frac{P_2^{\frac{\gamma-1}{\gamma}}}{P_1} - 1}{\Delta T/T_1}$$

Simple algebra transposition results in an expression which is useful when assessing the parameters that affect the stage pressure ratio:

$$\text{OPR} = \left(1 + \frac{\eta_{is}\Delta T}{T_1}\right)^{\frac{\gamma}{\gamma-1}} = \left(1 + \frac{\eta_{is} \frac{UV_\alpha}{C_p} (\tan a_1 - \tan a_2)}{T_1}\right)^{\frac{\gamma}{\gamma-1}}$$

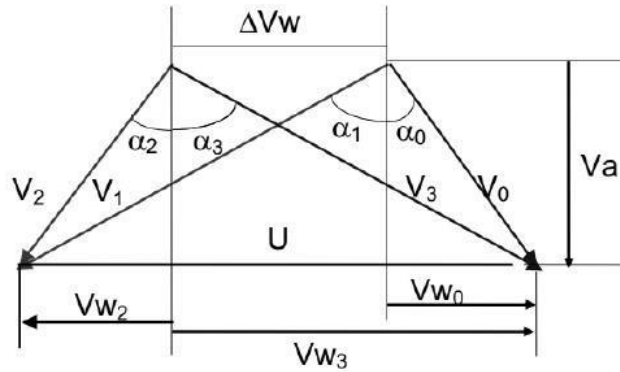


Figure 3: Combined velocity triangles (5)

It is common in engineering practice to use non dimensional performance parameters. Compressor designers use two very important dimensionless parameters to review preliminary design feasibility - the stage loading coefficient and the flow coefficient.

The stage loading coefficient is defined as the difference in total specific enthalpy against the square of the blade speed and it is a measure of energy exchange per unit mass flow for a given blade speed:

$$\psi = \frac{\Delta H}{U^2}$$

It follows that a high value of ΔH implies a high value of ψ . In other words, as the PR rises so does the stage loading coefficient. At the tip of a blade which is subject to a constant pressure ratio spanwise, ψ is not critical. However, at the root of the blade ψ increases and it may be necessary to reduce the pressure ratio at the hub to avoid overloading. (8). Typical values for the stage loading coefficient can be anything from 0.5 to 1.2 (5).

The flow coefficient is defined as the axial velocity over the blade speed:

$$\varphi = \frac{V_\alpha}{U}$$

and from continuity $W = \rho A V_a$, it can be considered as a measure of the mass flow, W , passing through a stage at a given blade speed.

2.1.3 Parameters affecting the pressure ratio

Blade speed

The blade speed, U , is a function of the rotational speed of the compressor, N , and the blade radius, r , and therefore the maximum blade speed occurs at the tip of the blade and is equal to $U_t = 2\pi N r_t$ where the suffix 't' refers to the tip.

Moreover, the centrifugal stress in the rotor airfoils depends on the speed of rotation and subsequently of the blade peripheral speed, the material of the airfoil and the size of the blade. Introducing the hub to tip ratio as r_h/r_t and assuming for simplicity that the blade cross section is constant from hub to tip, the maximum centrifugal stress will take place at the hub of the blade and is given by the equation that follows (3):

$$(\sigma_{ct})_{\max} = \frac{\rho_b}{2} U_t^2 \left(1 - \frac{r_h^2}{r_t^2}\right)$$

Where ρ_b is the density of the material. It becomes obvious that the centrifugal stress is proportional to the square of the blade tip speed and is a limiting factor. Tip blade speeds around 350 m/s are usually not critical to the sizing of the annulus (3). However, to avoid possible blade failures due to centrifugal stresses, the current maximum stress limit sets the maximum blade tip speed at 450 m/s (5).

Axial velocity

Equations (4.11) and (4.14) make obvious the utility of a high axial velocity in achieving a high compressor pressure ratio. Continuity also implies that a high axial velocity is required to acquire a high flow rate per unit frontal area.

Considering the first stage of a compressor without NGVs, where air enters axially (i.e. $\alpha_0 = 0$) the following expression can be derived from the velocity triangles. (Figure 3)

$$V_1^2 = V_\alpha^2 + U^2$$

Assuming a constant axial velocity over the blade height, the maximum relative velocity will also occur at the tip of the blade. For a given U_t , it follows that the rotor inlet relative Mach number will be directly proportional to the inlet axial velocity (3). Axial velocities for industrial gas turbines are of the order of 150 m/s, whilst state of the art aero engines can reach values up to 250 m/s (5).

Fluid deflection angles

The difference between the inlet and outlet swirl (or the swirl velocity angles) defines the amount of deflection required to achieve the desired pressure ratio of the compressor stage. In other words, the higher the fluid deflection, the higher the diffusion rate. Ideally, compressor designers would design their diffusers maximising the pressure ratio since that would imply more compact, simpler and cheaper to design and produce turbomachinery. Real diffusers however are far from ideal. The molecules of air cannot accommodate very high pressure ratios, for the surface boundary layer would be subjected to exceedingly high shear stresses that would force the flow to detach and would result in high separation losses. A tool that allows the designer to assess the permissible diffusion is the de Haller number, defined as $dH = V_2/V_1$. Low values of de Haller number result in excessive losses (3).

Adverse pressure gradients set the limit of allowable pressure rise across the blade row as following (5):

$$\frac{\Delta p}{\frac{1}{2} \rho_1 V_1^2} = 1 - \frac{V_2^2}{V_1^2} < 0.58$$

Which gives a value for de Haller number:

$$dH = \frac{V_2}{V_1} > 0.65$$

Kopanakis (9) in his MSc thesis reports that there are blades in operation today with de Haller number as low as 0.6.

This is a very simple method of assessing the diffusion. Nonetheless is still in use during the preliminary design phase. A more accurate design criterion was created by NACA using cascade testing data and is preferred for final design calculations. The so called diffusion factor.

To better explain the diffusion factor it is worth gaining an insight into the flow around a compressor blade. The air passing over the airfoil will experience an acceleration on the suction side (SS) of the blade which will result to a static pressure drop. On the pressure side (PS) the fluid will decelerate. Figure 4 depicts a typical velocity distribution through the passage. The maximum velocity appearing on the SS takes place at around 10-15% of the chord from the LE and then the flow decelerates steadily until the outlet velocity is reached. It has been shown, that the losses in a blade row arise mainly due to the PS and SS surface boundary layers' growth. These layers meet at the TE and form a wake which results in a total pressure drop. Thick boundary layers occur in regions of high velocity gradients and result in high losses.

Based on a large number of cascade tests the NACA diffusion factor, DF , can be expressed as:

$$DF \approx \frac{V_{max} - V_2}{V_1} = 1 - \frac{V_2}{V_1} + \frac{\Delta V_w s}{2V c}$$

Where; s is the pitch and c is the chord of the blade as illustrated in Figure 4 below. It has been reported that for the hub section of an airfoil, the losses are not affected noticeably for DF values lower than 0.6. In the tip section on the other hand, the losses increase greatly for DF over 0.45 (3) (5).

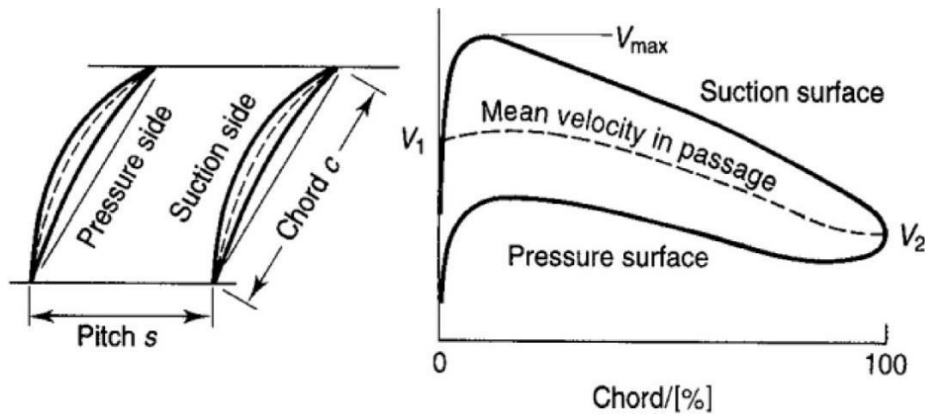


Figure 4: Blade spacing and velocity distribution through passage (3)

2.1.4 Blockage factor

Due to the adverse pressure gradient that occur, the boundary layers along the annulus walls become thicker across the compressor. This results in a reduction of the available area for flow. This effect inevitably affects the axial velocity of the fluid and thus, should be taken into consideration during the design process (3). This means that an increased

design annulus area should be chosen, in order to compensate for the reduced work that would be achieved (5) as can be seen in the diagram below. The complexity of the flow within a gas turbine (successive accelerations and decelerations, tip clearance, shock waves etc.) makes the calculation of boundary layer growth practically impossible and for that reason engineers are using empirical correction factors based on experimental data from compressor tests.

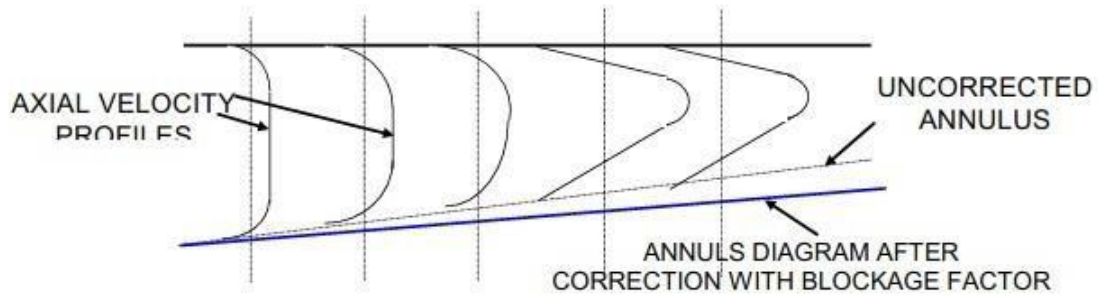


Figure 5: Blockage factor annulus correction (5)

Typical values of blockage factor can be found in Table 1:

Table 1: Typical values of blockage factor (5)

Stage number		1	2	3	4	5+
K_B		0.99	0.95	0.92	0.9	0.88

Where the blockage factor is defined by the following expression:

$$K_B = \frac{A_{ANN \text{ for uniform } V_\alpha}}{A_{ANN \text{ for NON uniform } V_\alpha}}$$

After the fifth stage it can be assumed that no further distortion of the axial velocity occurs and therefore the same blockage factor should be used for any remaining stages.

2.1.5 Annulus configuration

The choice of annulus configuration depends mainly on the size restrictions of the engine and the mean diameter requirements of the adjoining compressors in multi-shaft configurations and for an axial flow compressor can be one of the following:

- Rising line (or constant tip diameter)
- Constant mean diameter
- Falling line (or constant hub diameter)

Figure 7: Compressor annulus configurations depicts the various annulus configurations for core compressors

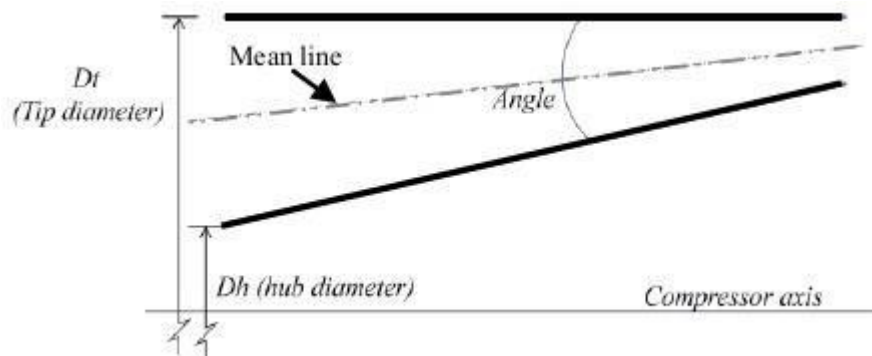


Figure 6: Typical compressor annulus diagram (10)

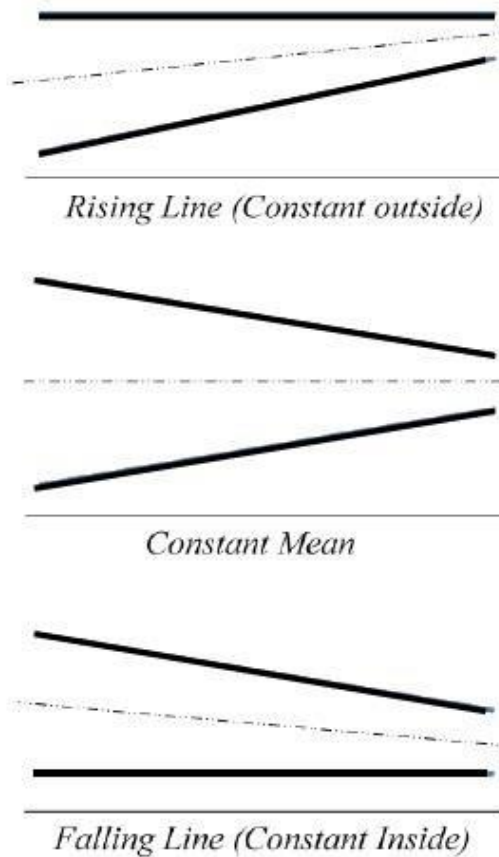


Figure 7: Compressor annulus configurations (10)

The rising line configuration for given mass flow generally gives lower outlet blade height and higher rear stage blade speeds and hub to tip ratio (D_h/D_t). This results to more tip leakage but the increased blade speed has beneficial effect on blading issues. The converse arguments stand for the falling line configuration. It is common practice to assume initially during the preliminary design stage a constant mean diameter annulus (5).

2.2 Design Process

The fundamental problem in the design of a turbomachine is the specification of a blade row that produces a desired energy or total pressure change with a given fluid flow rate. Due to possible restrictions on the size, efficiency, operating characteristics, and cost of the turbomachine, additional constraints on the size, speed, and type of blade row may be necessary. The problem the designer faces is the optimization of the blade row with respect to these constraints while still achieving the desired over-all performance. The design of a turbomachine is accomplished in several fairly distinct but interactive phases. As progress from one step to the next is made, the possibility of iterations and back steps is always at hand if it becomes obvious that some portion of the design will not fit the performance specifications (11).

The gas turbine engine design process starts with specifying certain criteria based on customer requirements and market research. Many factors have to be considered depending on the application. Apart from the required power and efficiency, the engine designers should take into consideration a variety of factors such as weight, cost, volume, life, emissions, noise etc. Many of these may be opposing each other. In addition, the design of the engine has to be done with future growth in mind, since customers will be demanding more powerful or more efficient versions also known as uprated engines. The development of a modern gas turbine engine is thus an extremely costly and tedious procedure which nowadays is usually shared between several companies.

The first step towards designing an engine is the thermodynamic design point study which entails detailed calculations over a range of pressure ratio and turbine inlet temperatures considering important factors such as air-bleeds, expected component efficiencies, pressure losses etc. In industry such calculations are carried out using sophisticated software. Taking into account both mechanical and aerodynamic design among others, a set of suitable parameters is selected and the thermodynamic design point study determines the airflow, the pressure ratio and turbine inlet temperature required to give the specified power.

Once this is done the design process continues with the aerodynamic design of the turbomachinery which defines annulus dimensions, rotational speeds and number of stages. Changes in the design point will inevitably occur due to changes in operating

conditions (varying ambient and flying conditions, reduced power operation etc.) and due to the gradual degradation of the engine and therefore off design performance should be taken into consideration at this point.

After both the thermodynamic and aerodynamic studies have taken place and the key dimensions of the engine have been established, the mechanical design of the gas turbine which deals with stress analysis, vibrations and material selection can begin.

Control system design and manufacturing feasibility need also to be taken into consideration. All these activities are inextricable linked and the final design of the engine can only come out of an iterative process which requires a continuous flow of information between the various specialists for each stage until the best compromise is found (3).

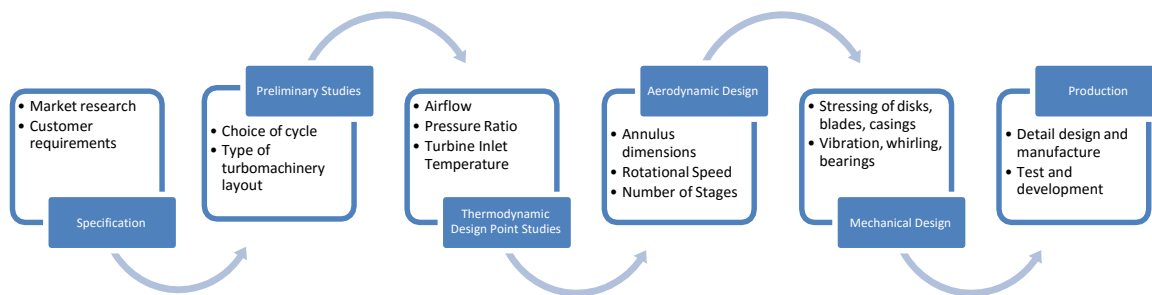


Figure 8: Typical gas turbine design procedure

The aerodynamic design process of an axial flow compressor, like the design of all gas turbine major components, is highly iterative and interactive and it makes use of a variety of tools, from simple mean line methods to most sophisticated 3D CFD. It can be simplistically split into four different phases: preliminary, through flow and blading (2D and 3D) design (12).

2.2.1 Preliminary Design

With the specification of the performance parameters and design constraints, the first phase, the preliminary design, is initiated. In this phase, the overall design and the main features of the compressor (a preliminary layout of the compressor geometry, basic blade row sizes and speed etc.) are determined. The performance specifications will also determine if axial, mixed, or radial flow blading is required (11). Relatively simple and fast tools are used to filter out the various possibilities before more sophisticated tools are used to assess the prevailing design options. It is the most

important step in the design process since any fundamental mistake, such as choosing too few stages or too short compressor, will not be amendable during the later stages and thus will have serious consequences. The basic inputs to the preliminary design stage are requirements regarding flow capacity, pressure ratio, efficiency and surge margin for a range of engine operating points. These should be achieved at appropriate shaft speeds for the turbomachinery components. Furthermore, mechanical restrictions regarding the compressor length and diameter to be compatible with the whole engine configuration have to be met (12).

The basic tools used at this step are mean line performance prediction programs that assume that the flow through the compressor is steady, inviscid and one-dimensional and in effect solve iteratively the mean velocity triangles through the compressor, until the calculated annulus, number of stages, blade numbers and flow angles are found to be satisfactory

2.2.2 Through Flow Design

The next stage is the detailed specification of the blade spanwise loading distribution. Empirical data impose a limit on the amount of work a single blade row can perform without severely affecting the blade's efficiency by causing stall or flow separation. An iteration with the initial design phase may be necessary to assure that the blade row will not be overloaded and perform poorly (11). Having established the optimal overall layout of the engine during the preliminary design phase, the development of a compressor design method requires an accurate model of the through-flow describing the spatial variation of the velocity and pressure in the fluid. The through flow surface, also known as the meridional plane is the 2D hub to tip blade representation and can be seen in Figure 9. Equations of motion are developed in a way that allows the representation of the blade row spanwise and chordwise. Due to the complexity of the governing equations, blockage and loss models are taken into consideration in an empirical fashion, to address the effects of endwall boundary layers, viscosity and turbulence (11).

There are various ways to implement through flow analysis in the design process. Initially simple radial equilibrium theory coupled with free, forced or free vortex methods, to take into consideration the radial variation in blade design calculations, was used extensively in the industry. However, application of simple radial equilibrium theory to

certain cases resulted in designs with unsatisfactory stall margins (13). Nowadays, codes capable of solving full radial equilibrium have been developed and methods like Streamline Curvature Method (SCM) are used extensively.

The SCM of through-flow refers to a technique that is used to develop the numerical model, solving the inviscid equations of motion for the flow and correcting the solution for the flow losses due to viscosity and turbulence that are expected. The detailed velocity and pressure fields are calculated, and by examination of these and the power requirements, corrections can be made either to the preliminary design, if necessary, or to the spanwise loading distribution (11). The SCM has been used successfully for the determination of the through-flow solution for axial flow pumps, compressors, and turbines. The result of this phase is a 2D model of the turbomachinery component that satisfies all of the design restraints and requirements and the laws of fluid motion.

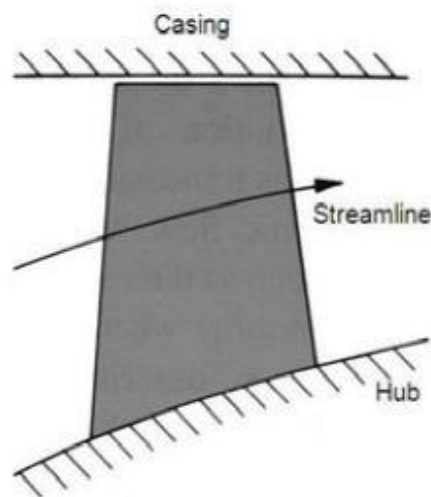


Figure 9: Blade meridional plane (13)

2.2.3 Blade to Blade Design

The final phase in the design is the specification of the actual blade geometry that will produce the flow field specified by the through flow analysis. This is the most difficult phase of the design problem as the real effects of viscosity and turbulence play a very important role in the actual performance of the blade row (11). The real flow is highly three dimensional and complex. The best models that can be used in the design are 2D blade sections stacked together along the spanwise direction to define full 3D blades (9). To that end, through-flow data at different radii are inputted in the Blade to Blade analysis, and using correlations for estimating various losses, incidence and deviation angles, the features and the shape of the final blade are estimated (13).

Having the blade geometry handy, examination of the flow field may reveal areas that have the propensity to produce undesirable flow phenomena (e.g. separation), indicating that adjustments must be made in the previous design phases. The predicted blade losses and flow angles can be fed back to the through flow analysis to produce further refined blade sections (13). The final acceptance of the design is then based on the mechanical strength of the blade and its suitability for manufacture. Again, additional iterations, going as far back as the preliminary design may be required (11).

2.2.4 Three Dimensional Analysis

With the advent of computer technology which results in cheaper and more powerful processors and with computational fluid dynamics software becoming more and more capable to simulate complex flow phenomena, CFD has become an absolutely necessary part of any turbomachinery design process, and succeeds in reducing both development time and cost. Up to this date CFD solvers for compressors are limited to solving RANS or Euler equations iteratively in order to simulate the 3D flow. However, in the near future with further advancements in computer technology, use of the more computationally demanding DNS and LES might become possible. CFD results, although credible, still need to be verified using experimental data (8).

2.3 Blade Geometry

Blading design is part of the compressor aerodynamic design process and is carried out to obtain the blade geometry and the number of blades that are required for each stage. Among others, the parameters required from the final design stage to be imputed to the blading design include: the inlet and outlet blade angles and Mach numbers. Figure 10 shows the cross section of a typical cascade and introduces the various parameters that are associated with cascade testing.

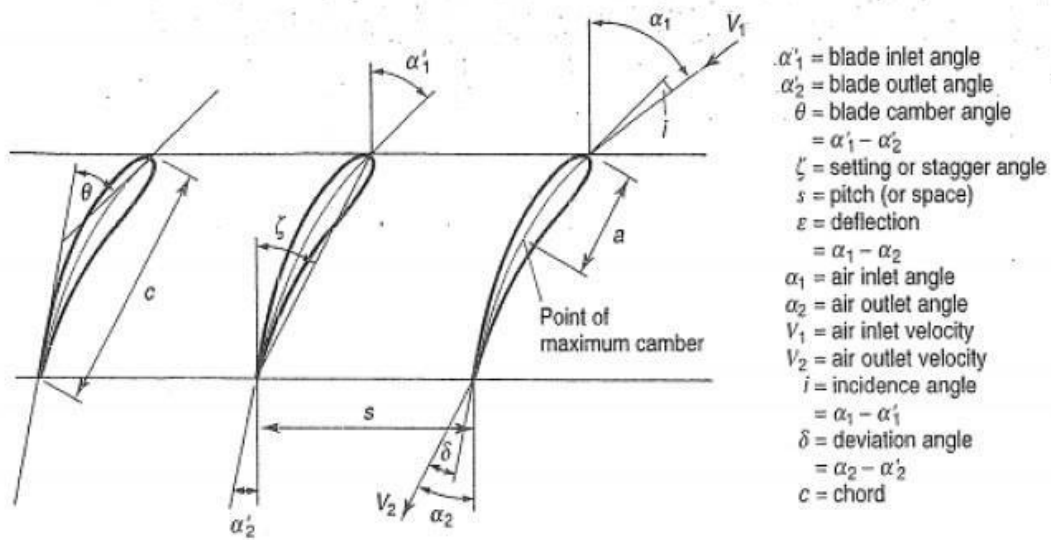


Figure 10: Cascade nomenclature (3)

Assumptions based on the type of aerofoil section and thickness to chord ratio (t/c) are made and estimations for the space to chord ratio (s/c) are also undertaken using Zweifel and Howell's methods of estimation. The mean value of these estimates is usually chosen (7).

Results obtained from blading design include the angles of incidence and deflection, deviation, stall margin, deflection factor, critical Mach number, throat margin, camber and stagger angle (10). Approximate limits for blading design values are shown in the table below.

The critical Mach number should be less than the design point Mach number to keep losses at an acceptable level. The blade chord is determined from the blade aspect ratio and blade height. The obtained chord is used to calculate the inter-blade spacing using the space to chord ratio, s/c . Therefore, the number of rotor and stator blades for each stage can be obtained.

2D and 3D analysis of the blade profiles are undertaken using advanced blade design models and computer codes as one means of validating the blade performance. An unsatisfactory estimated blade performance will lead to modification of the blade design to achieve the optimum possible performance. Blading design for a low pressure compressor can be found in later chapter (10).

2.3.1 Incidence angle

The incidence angle is defined as the difference between the air relative inlet angle and the blade inlet angle at the LE and for a subsonic cascade can be calculated using the following expression (9):

$$i = K - 0.19\theta \frac{s}{c}$$

Where K equals 6.5 for a rotor row and 3.5 for a stator respectively. During cascade tests the pressure and direction measuring instruments are located upstream and downstream of the blade row and they measure the deflection of the air:

$$\varepsilon = \alpha_1 - \alpha_2$$

and the variation of loss in stagnation pressure which can be represented by the loss coefficient, calculated as:

$$\omega = \frac{P_1 - P_2}{P_1 - p_1}$$

where the parameter P stands for the stagnation pressure and p for the static pressure, whilst the index 1 refers to the measurements taken prior to the blade row and 2 after it. Based on experimental data, correlations are taken into consideration to define critical blade design parameters such as the minimum loss, stall and stagnation point. Such results for a blade cascade which has $s/c=0.67$, $\theta=41.06$ and $\zeta=-22.17$ can be seen in Figure 11. It is difficult to predict the exact incidence at which stall occurs, therefore the stalling incidence is defined as the incidence at which the mean stagnation loss becomes equal to twice the minimum loss (9).

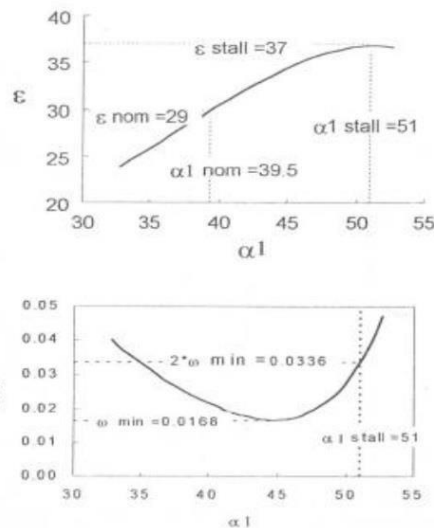


Figure 11: Deflection and Loss coefficient against air inlet angle (9)

2.3.2 Deviation angle

Ideally, the air leaving the blade row would be that of the blade metal angle at the TE. In reality it has been found that there is a loss in deflection defined as the deviation, δ , due to the resistance of the air to follow the exact path required by the airfoil shape. It has been seen through cascade tests, that there is a relation between deviation and the blade camber and pitch to chord ratio which can be summed up in the following expression, also known as Carter's rule:

$$\delta = m\theta \sqrt{\frac{s}{c}}$$

where m is a function of the stagger angle, ζ , equal to:

$$m = 0.126 + (1.823 \cdot 10^{-3})\zeta + (2.14 \cdot 10^{-5})\zeta^2 \text{ for NACA 65-series and}$$

$$m = 0.126 + (9.72 \cdot 10^{-4})\zeta + (2.38 \cdot 10^{-5})\zeta^2 \text{ for C-series and DCA (9)}$$

2.4 Axial flow compressor blade profile families

Until recently, the traditional approach to axial-flow compressor aerodynamic design was to make use of various blade families as the basis for airfoil design. Americans use various families defined by NACA, the most notable example of those being the 65-series family. Similarly, British practice is based on the C- series families, using circular-arc or parabolic-arc camberlines. Later on, as design requirements began to favour transonic compressors, DCA and MCA blades became popular. The performance characteristics of these blade profile families are well understood thanks to extensive experimental cascade testing, much of which is available in the literature. Nowadays, instead of using predefined airfoil families, blades specifically designed for a prescribed surface velocity distribution or blade loading style, have become increasingly popular. Often, inverse design methods that predict the blade shape required for the desired blade loading are used. As the relation between blade shape and preferred loading styles became better understood, it also became common to use conventional or direct analysis methods in a trial-and-error mode to arrive at the same result. These airfoils have been referred to as prescribed velocity distribution (PDF) blades, even though the term controlled diffusion airfoils is probably more common today (14).

2.4.1 NACA 65-Series

NACA 65-series aircraft wing airfoils were developed by the American National Advisory Committee for Aeronautics and were originally designed for uniform blade loading. The basic profile has its maximum thickness located at 40% of the chord and is very thin towards the TE raising questions regarding its structural integrity. To address this issue several adaptations of the original profile thickness distribution are used today. NACA 65-series blades are specified by their lift coefficient and maximum thickness to chord ratio. The lift coefficient appears first in tenths in a parenthesis and the thickness to chord ratio follows as a percentage.

E.g. a 10% thick blade with a lift coefficient equal to 1.5 is nominated as NACA 65-(15)10 (14).

2.4.2 British C-series

The British have developed the C-series blade profiles mainly for subsonic applications. Several series are found in this category, with C.4 series being a notable example for its performance characteristics. Compared to the NACA 65- series the C.4 profile is thicker toward the LE and the TE and its maximum thickness is located at 30% of the chord. This implies that the C.4 airfoil is less effective for higher Mach number applications but it offers structural integrity advantages. A later series, i.e. C.7, was developed mainly for compressors and shares many features with the NACA 65-series (14).

2.4.3 Double Circular Arc

Transonic blading demands thin LE and TE to minimise shock and wake losses. DCA profiles have their maximum thickness located at the middle of the chord and their LE and TE are formed by semi-circular arcs with thickness equal to 6% of the maximum thickness. The PS and the SS are both formed by circular arcs and it has been reported that DCA profiles have a much wider minimum loss incidence than the C.4 profiles.

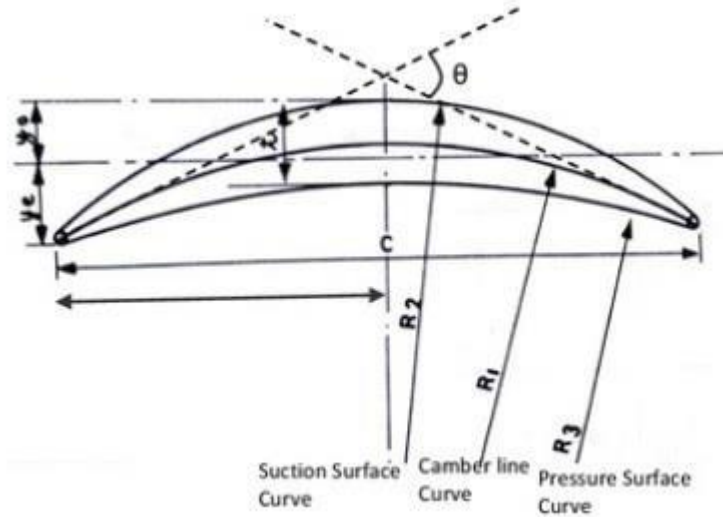


Figure 12: DCA typical profile (13)

Figure 12 shows a typical DCA airfoil profile. LE and TE angles are derived from blade angles calculations and according to diffusion factor and chord length requirements the camber line tangent to LE and TE angle is created. Then the PS and SS derive by offsetting the camber line curvature according to maximum thickness requirements. Finally, the PS and SS curves are joined with circular arcs at LE and TE.

Figure 13 illustrates a comparison of the pressure coefficient against the chord length between the three blades described up to this point. It can be seen that the NACA 65-series achieve the highest pressure recovery. Both NACA 65 and C.4 profiles have a low pressure region near the LE which implies that the local boundary layer is decelerated. Deceleration of high velocity flows is linked with losses and flow separation. DCA profile shows an acceleration of the flow near the SS LE along with an increasing adverse pressure gradient, that result in a much more satisfactory static pressure recovery (13).

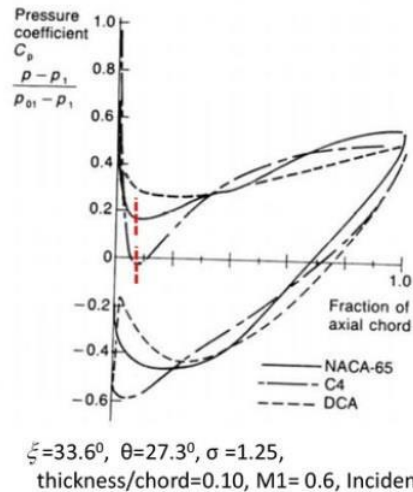


Figure 13: Pressure distribution comparison (13)

2.4.4 Multiple Circular Arc

MCA profile airfoils derived from the DCA and are used in transonic applications. Not unlike their predecessors, the camber line of the MCA airfoils is composed of two circular arcs and their profile shape is given by superimposing this camber line and their thickness distribution.

2.5 Rotor 37

NASA Rotor 37 is an isolated transonic axial flow compressor rotor with 36 blades that was used as a test case for turbomachinery CFD by the IGTI to test the capacity and reliability of 3D flow solvers. Several blind solutions have been submitted and compared afterwards with the experimental results provided by NASA Lewis Research Center (21). For that reason, it is a very well documented case. The Rotor 37 geometry can be readily found in ANSYS documentation, which is accessible by password through the ANSYS Customer Portal using Cranfield student credentials. The availability of the geometry and the plethora of open source experimental and simulated data that can be used for CFD model validation lead the author to choose Rotor 37 as his baseline geometry.

Test case details

The Rotor 37 case was part of a larger project that aimed to cover a wide range of typical gas turbine engine design parameters and was presented in the AGARD Advisory Report 355 under the title ‘CFD Validation for Propulsion System Components’ (21). All the experimental data that are available in the public domain

were measured with the Rotor 37 operating under its design rotational speed that is equal to 17188.7 rpm. NASA reported that the experimental choked mass flow was $W_{choke} = 20.93 \text{ kg/s}$ and the near stall mass flow was $W_{stall} = 0.925 W_{choke} = 19.36 \text{ kg/s}$. Within this mass flow range a number of measurements were carried out in four hub-to-tip measuring planes. The first of these planes is located 4.19 cm upstream of the blade LE and radial profiles of total pressure and temperature are available publicly and can be used as inlet boundary conditions. Figure 14 shows a meridional view of the flow path along with the four measuring planes.

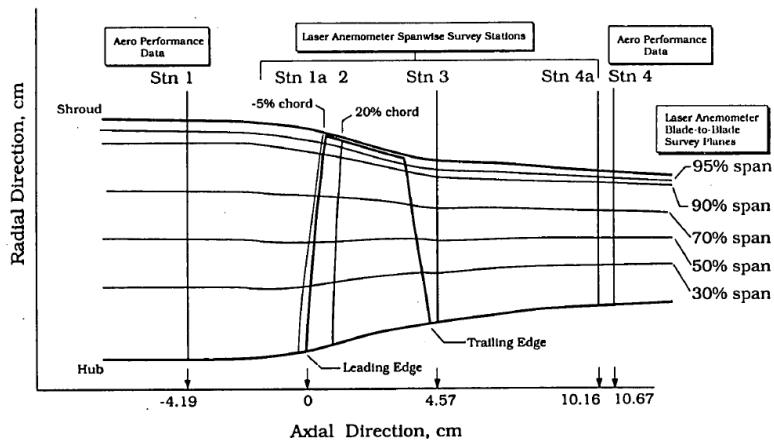


figure 14: Rotor 37 measurement stations (22)

Table 2: Rotor 37 inlet boundary conditions (22)

Radius (cm)	Absolute total pressure (Pa)	Absolute total temperature (K)
17.9222	99946.98	288.265
18.3490	101740.43	287.862
18.7452	101872.15	287.775
19.1414	101872.15	287.804
19.5682	101872.15	287.804
19.9644	101872.15	287.804
20.5435	101872.15	287.862
21.0922	101872.15	287.977
21.6713	101811.36	288.035
22.2504	101740.43	288.265
22.7990	101669.50	288.381
23.2258	101740.43	288.323
23.6220	101811.36	288.208
24.0182	101740.43	288.150
24.4450	101527.65	288.208
24.8412	100909.56	288.265
25.1765	98913.46	288.265
25.4203	95600.13	288.381

Table 3 summarises the main aerodynamic parameters as they are given by Denton (21).

Table 3: Basic aerodynamic design parameters

Parameter	Value	Unit
Number of blades	36	-
Tip diameter at LE	0.5074	m
Hub diameter at LE	0.3576	m
Rotational speed	17188.7	rpm
Tip solidity	1.288	-
Tip Clearance	0.356	mm
Tip speed	454.14	m/s
Pressure Ratio	20.106	-
Mass flow rate	20.19	kg/s
Blading	MCA	-

3 3D MODEL GENERATION FOR CFD ANALYSIS

3.1 Introduction

Even though the equations that govern the flow of any fluid have been known for almost two centuries, their analytical solution has not yet come to pass. These equations, known as the Navier-Stokes equations, form a complex set of partial differential equations and have their basis in three fundamental physical laws. Namely the conservation of mass, momentum and energy. CFD is the art of obtaining a numerical solution to fluid flow problems with the aid of computers. Thus, CFD provides a very useful insight into the abstruse flow phenomena that are present in gas turbine engines and has become an indispensable part of their design process and certification (23). It is worth noting that until recently the design process of an aircraft engine required 90% of rig testing and 10% of CFD simulations. Nowadays these figures are almost inverted (24). It is not the scope of this study to understand and explain in detail the theory behind CFD applications. The reader who desires a better understanding of this mathematically sophisticate engineering domain will a find a valuable resource in Tu's Computational Fluid Dynamics: A practical approach (25).

To carry out the CFD study ANSYS Workbench, which combines powerful solvers with useful project management tools, was used. ANSYS Workbench platform was chosen because it allows users to set up complete turbomachinery analyses, from geometry design to meshing, with persistent system-wide parameter management to automate the entire standardized processes. The baseline geometry and its subsequent modifications necessary for this study was created using ANSYS BladeGen. ANSYS Turbogrid was selected to generate the grid. CFX Pre-processor was used to set up the numerical model (boundary conditions and fluid properties). Then CFX solver obtained the solution and was analysed with the help of CFX Post-processor.

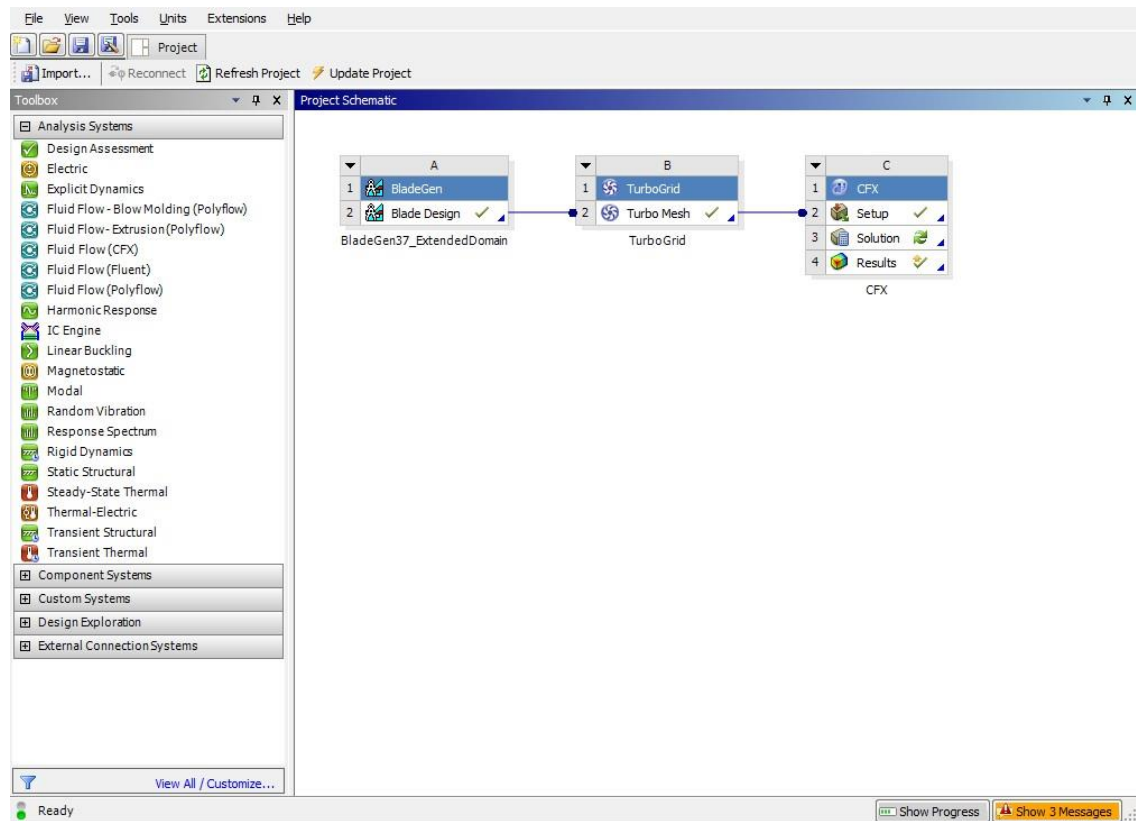


Figure 15: ANSYS Workbench Project Schematic

3.2 The CFD modelling process

From the definition of the flow problem to the final findings report, certain steps have to be undertaken bearing in mind that the main objective is to obtain repeatable results with a quantified error (26). These basic steps are:

- 1) Physical scenario
- 2) Geometry
- 3) Computational Mesh
- 4) Governing Equations
- 5) Physical Models
- 6) Solution Algorithm
- 7) Boundary Conditions
- 8) Obtain Solution
- 9) Analysis

Figure 15 illustrates schematically the main parts of the CFD simulation procedure.

The following sections of this chapter discuss the actions taken towards the completion of each of these steps.

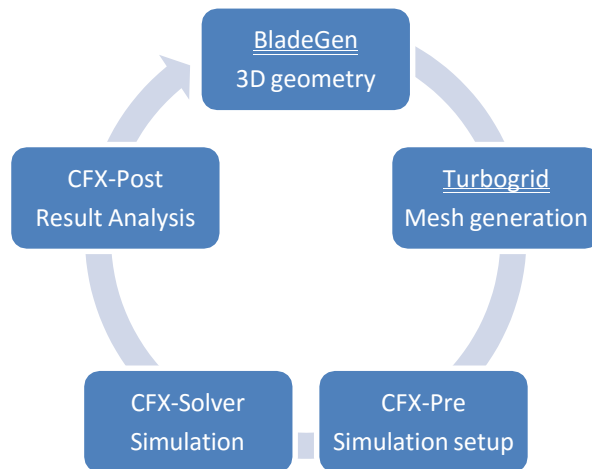


Figure 16: Simulation procedure

3.3 Defining the 3D Geometry

Having decided the case study of NASA Rotor 37 and the manufacturing modifications that are to be assessed, the first step towards the completion of the CFD analysis is the modelling of the geometry. ANSYS BladeGen was used to create the 3D model. BladeGen is an advanced blade modelling software that comes with an interactive GUI that facilitates the design of a wide variety of turbomachinery components. It was chosen because it allows the user to easily modify the geometry, once it has been established, simply by adjusting a number of well-known blade design parameters. Geometry files for Rotor 37 were readily available in ANSYS documentation data and consist of three curve files that contain the geometry information in lists of polar coordinates. Using ANSYS BladeGen Data Import Wizard to load the curve files, the curvature of the hub, shroud, and a single blade are defined and the 3D model of the blade is automatically generated.

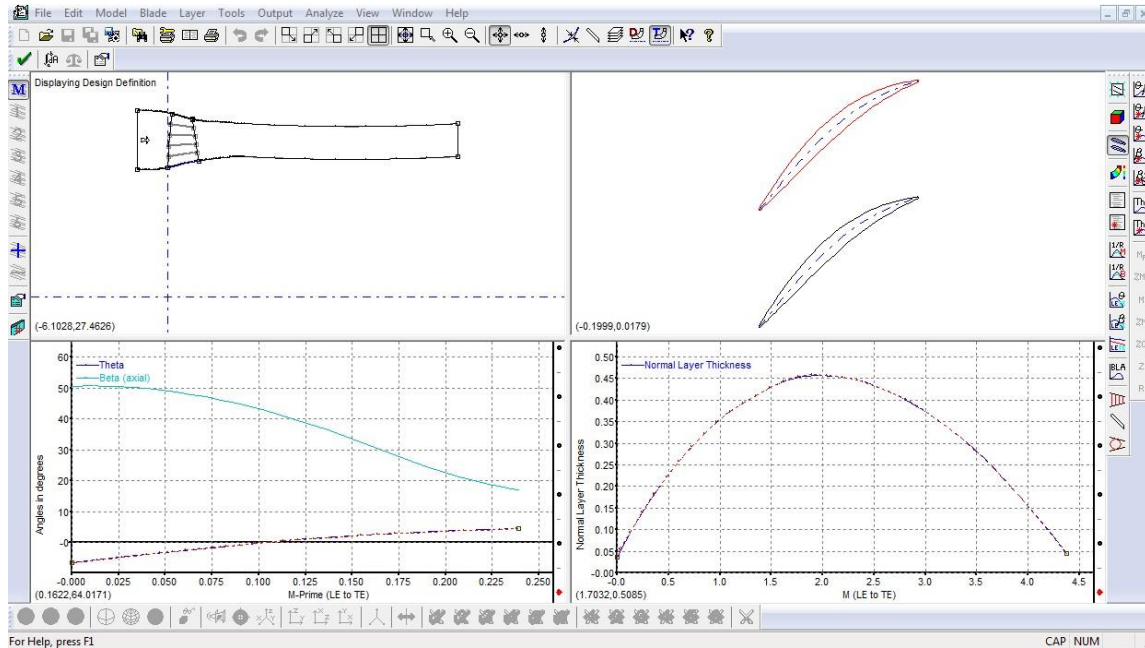


Figure 17: BladeGen GUI

Zhub

31 points

```
-22.860001 -17.779999 -12.700000 -7.620000 -3.070860 -2.435860 -1.800860
-1.165860
-0.264160 0.101600 0.736600 1.371600 2.006600 2.644140 3.279140
3.914140
4.521200 5.153660 5.788660 6.423660 7.058660 7.693660 8.328660
8.963660
9.598660 10.233660 10.868659 11.503659 12.138659 12.646660 15.240000
```

Rhub

31 points

```
17.525999 17.525999 17.525999 17.525999 17.525999 17.541241 17.571720
17.602200
17.739361 17.805401 17.957800 18.122900 18.298161 18.440401 18.567400
18.674080
18.768059 18.867119 18.948400 19.029680 19.110960 19.177000 19.235420
19.293840
19.329399 19.364960 19.390360 19.405600 19.420839 19.433540 19.433540
```

Figure 18: NASA Rotor 37 hub geometry file (23)

During this step the computational domain, i.e. the volume where fluid flow will take place, is also defined. It is of great importance to have a computational domain long enough to allow the flow to stabilize before and after the passage. For that reason, it is common practice to keep domain boundaries well away from the blade edges. Dr. Teixeira suggests that the domain inlet boundary should be located at least 1 blade chord equivalent length prior to the blade LE. Similarly the domain outlet boundary should be located more than 1.5 chord lengths after the blade TE (23). It was found at a later stage that such domain boundaries could not make allowance for the flow to stabilise and the solution could not converge, probably due to the complexity of the flow phenomena that occur in the Rotor 37 case (high Mach numbers, Shock waves,

wakes etc.). To address this issue, the outlet domain boundary was moved further downstream to an equivalent of seven chord lengths.

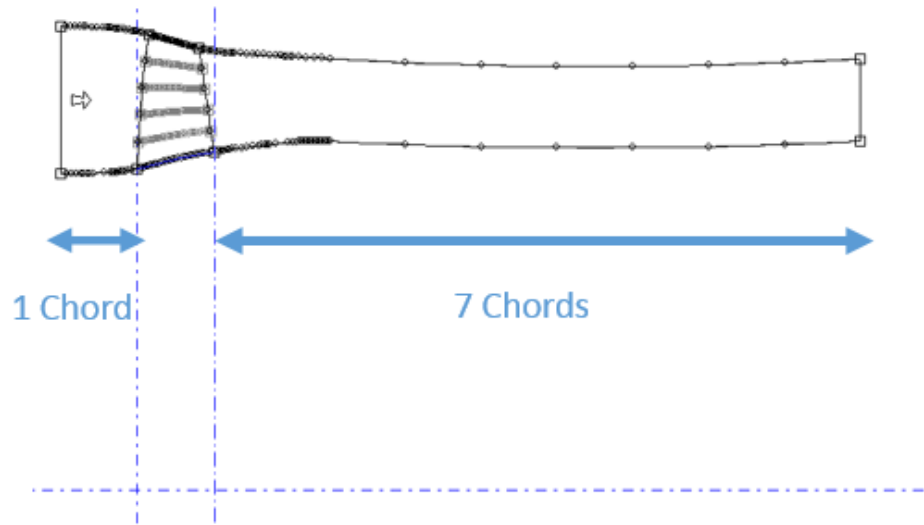


Figure 27: Rotor 37 computational domain

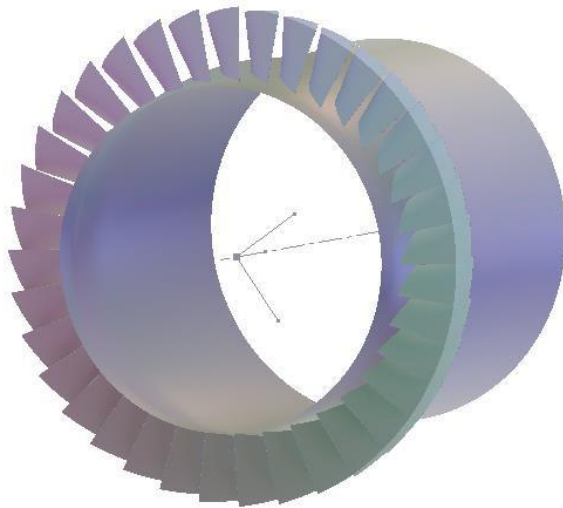


Figure 28: Rotor 37 3D model

3.4 Grid Generation

Within the computational domain a grid, which consists of finite control volumes, is generated. The governing CFD equations are then discretized and solved iteratively for each control volume. Accuracy, convergence and computational time of the simulation, all depend on the grid quality and density, making the grid generation one of the most important steps of the CFD process. It is also worth noting that the CFD user has the most influence over the solution via the grid.

ANSYS TurboGrid, a very popular meshing software among turbomachinery engineers, was chosen to create the grid of Rotor 37. ANSYS TurboGrid generates high-quality hexahedral structured meshes tailored especially for bladed geometries. The structured mesh enables the user to control the number of the nodes (i.e. grid points), reduces the need for computer memory in comparison with the unstructured ones, and is generally more tolerant of skew and stretching. It does however require a lengthier generation process and considerable user experience. TurboGrid features allow the creation of structured meshes with minimum user input.

Having the geometry defined, the following step was to define the topology that governs the general way in which the mesh is generated (27). The selected software has integrated grid topologies that ensure the creation of an optimal mesh. Using ANSYS TurboGrid object selector a Traditional, H/J/C/L-Grid Topology Set was applied as this is the recommended practice (13). H/J/C/L-Grid allows a separate choice of topology type for the upstream and downstream ends of the passage mesh. The decisions are automatic by default. An O-Grid, a topology that forms a continuous loop around the blade profile, was also selected since it yields excellent boundary layer resolution and near-orthogonal elements on the blade. The same topology will automatically adapt at a later stage to variants of the baseline design, ensuring that the mesh produced is consistent. Such self-consistent meshes are very convenient for assessing differences in performance predictions between various designs since they minimize the mesh dependency in any such comparisons and the user workload.

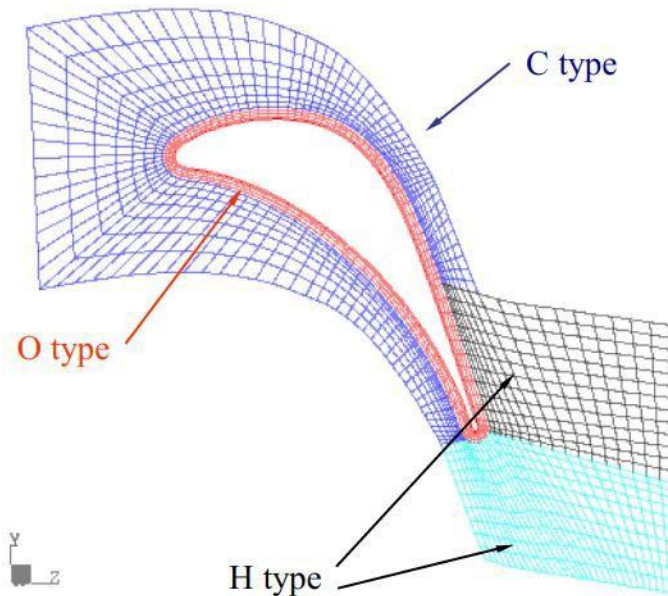


Figure 29: Multiblock steam turbine stator grid containing H, O and C grid types (23)

The mesh density is required to be fine enough to accurately resolve flow details of the wall boundary layer, both at airfoil and end wall surfaces. In order to capture the boundary layer, it is required to resolve the region around the blade. This was effectively achieved by including the O-Grid topology. The dimensionless wall distance, y^+ (also referred to simply as y plus) is commonly used in boundary layer theory and provides a tool to quantify the resolution of the boundary layer (28). It represents the distance of the first node from the nearest wall and depends on upstream Reynolds number and characteristic length (blade chord). To effectively capture the details of the wall boundary layer it is required to have the first node within the laminar (or viscous) sublayer. A y plus factor less than one can be perceived as a general guideline to achieve this resolution. When using wall functions, the mesh size requirement for capturing overall performance characteristics is $1-3 \times 10^5$ carefully chosen nodes. To describe more detailed flow phenomena such as endwall secondary flows or tip clearance the requirement rises to $5-10 \times 10^5$, whilst in literature grid independence at about $20-30 \times 10^5$ has been reported. Resolved boundary layers, low Re models, may require twice, even thrice, the above numbers (23). A compromise between mesh density and computational time/ resources requirements had to be made. The user has the ability to control the number and distribution of the mesh elements via the Mesh Data Object. A Target Passage Mesh Size of 5×10^5 elements was specified and an O-Grid factor of 0.3 was selected by the author as the best compromise for this study.

3.4.1 Grid quality assessment

The quality of the mesh is the most critical element of the simulation in terms of obtaining the best possible results and thus it is worthwhile to invest a considerable time in the grid generation process.

CFX software provides the following measures to describe the quality of the generated mesh:

Smoothness

This measure is related to the stretching (i.e. the ratio of distances between neighbouring grid points along a grid line) and should not exceed 35%. To minimise numerical errors by avoiding sharp discontinuities stretching less than 20% is required (23).

Skewness

By default, a value of 20 degrees is set in CFX as the maximum value of skew which does not result in solution accuracy deterioration. A value between 20 and 10 will result in some solution accuracy and convergence performance penalty. Any value below ten degrees should be treated as error condition and the mesh should be regenerated.

Aspect Ratio

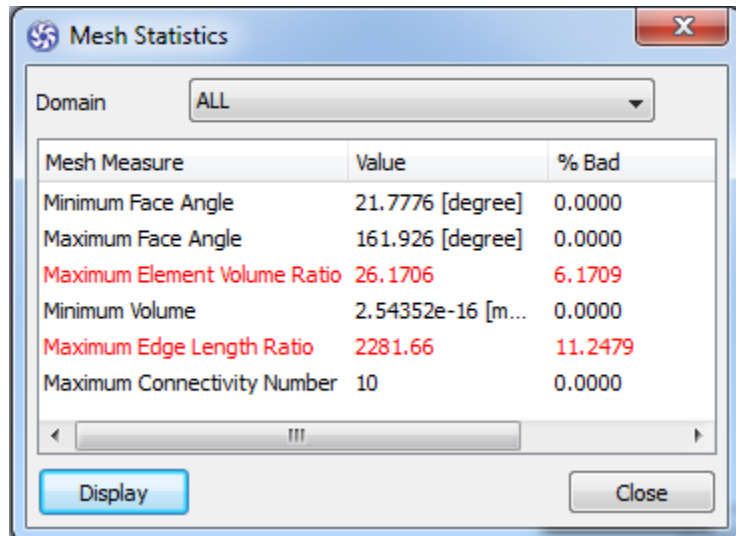
In CFX the Aspect Ratio limit is set at 100. Other codes may impose a stricter limit with 10 being a common value.

Alignment of grid lines with flow direction

Succeeding in aligning the grid lines with the local flow streamlines helps the reduction of numerical diffusion and the code manual highly recommends it.

Figure 19 shows the 3D mesh measures quality criteria as they are calculated by TurboGrid. In case a mesh measure fails to meet the criteria, Mesh Analysis > Mesh Statistics (Error) will appear in red text in the object selector. With default criteria, there will almost always be some mesh elements that fall outside the criteria; a visual inspection of the mesh measures is usually required to determine whether the mesh is satisfactory. It can be seen that Maximum Element Volume Ratio and Maximum Edge

Length Ratio do not meet the criteria. Note that not all of the mesh statistics have the same importance. E.g., it's necessary to have a mesh with no negative volumes. Generally, poor angles should also be fixed, but the Maximum Element Volume Ratio and Maximum Edge Length Ratio values should be judged based on the requirements of each case. The mesh that was generated was found to be satisfactory for the needs of this study.



Mesh Measure	Value	% Bad
Minimum Face Angle	21.7776 [degree]	0.0000
Maximum Face Angle	161.926 [degree]	0.0000
Maximum Element Volume Ratio	26.1706	6.1709
Minimum Volume	2.54352e-16 [m...]	0.0000
Maximum Edge Length Ratio	2281.66	11.2479
Maximum Connectivity Number	10	0.0000

Figure 19: Mesh statistics

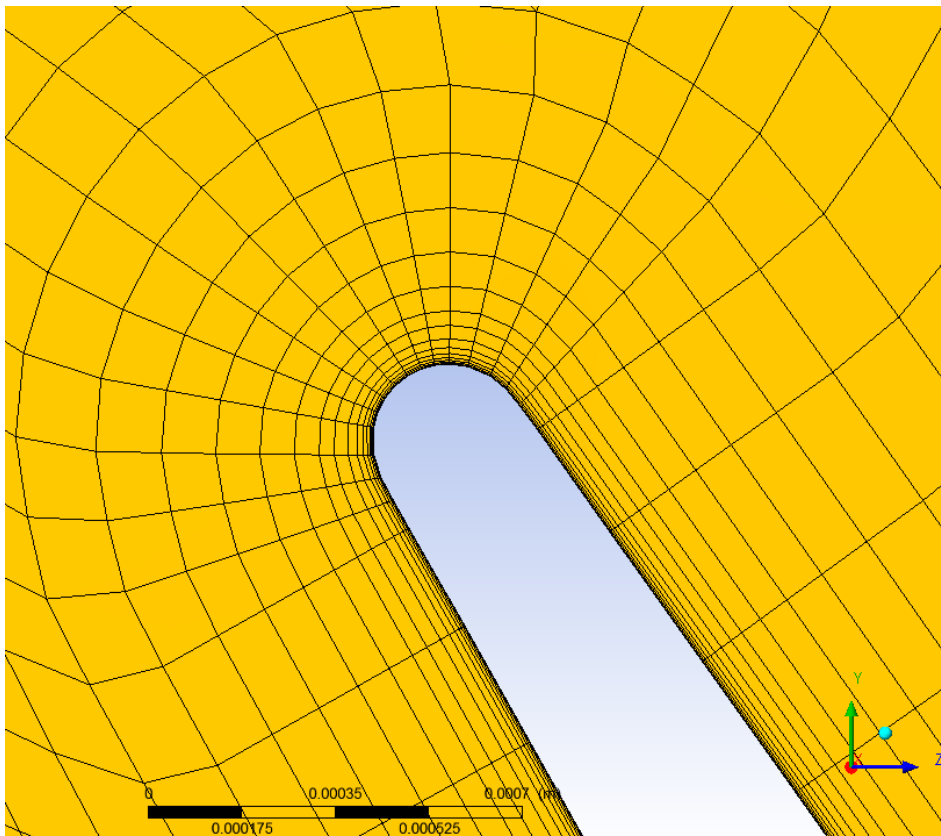


Figure 20: Observing the midspan Leading Edge O-Grid

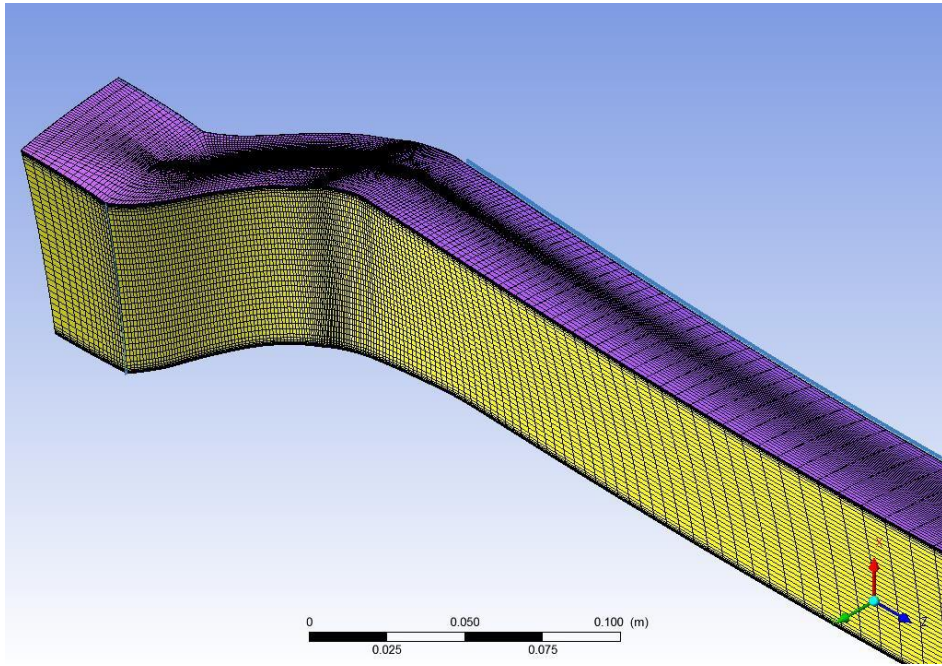


Figure 21: Meshed domain

3.5 Set up of the CFD simulation

In this section the specification of the boundary and initial conditions and the setup of the CFD simulation using CFX-Pre software, the physics definition pre-processor for ANSYS CFX, are described.

3.5.1 Specification of the boundary and initial conditions

In order to solve the partial differential equations that describe the fluid flow numerically, a set of additional constraints has to be provided. These constraints, also known as boundary conditions, are classified by CFX-Pre in certain categories according to their point of reference.

The 'Physics Definition' boundary conditions refer to the data used to define the fluid properties at the inlet and the outlet of the computational domain. CFX-Pre provides the user with the ability to select a set of predetermined Inflow/ Outflow Boundary Templates under the Physics Definition Tab. This happens to prevent over definition of the flow. The available combinations from the most robust to the least are (23):

Mass Flow Inlet, P-Static Outlet (Most robust); the P-Total Inlet is an implicit result of the prediction

P-Total Inlet, Mass Flow Outlet (Robust); the P-Static Outlet and the velocity at the inlet are part of the solution

P-Total Inlet, P-Static Outlet (Sensitive to initial guess); the system Mass Flow is part of the Solution

For this study several CFD simulations were undertaken. Some of them were making use of the second combination, whilst others - in order to predict the working line of the compressor - of the third. ISA SLS conditions (i.e. P-Total =101.325 kPa and T-Total = 288.15) were applied at the Inlet and the velocity was considered axial and as such the Flow Direction was set Normal to Boundary. The fluid was set to Air Ideal Gas and the Reference Pressure was considered negligible.

The experimental choke mass flow measured by NASA was 20.93 kg/s. The majority of the available data for this case were measured with the NASA Rotor 37 operating at the design rotational speed of 17188.7 rpm and refer to a mass flow equal to 0.98 times the experimental choke mass flow. For this study the Per Machine Mass Flow that was set as

the boundary condition at the domain outlet was Mass Flow Rate = 20.19 kg/s, which is the Rotor 37 corrected Mass Flow provided by Denton (20).

The 'Boundary Definition' boundary conditions characterise the interactions between the flow and the walls. For the hub and blade surfaces that are rotating machinery, the most realistic option was to set them as 'no slip walls' which implies that on the solid surfaces the velocity is nil. Note that the rotational speed has been imposed to the whole Rotor 37 domain. When it comes to the shroud surface, it was considered as a 'counter rotating wall', which means that the shroud rotates with a velocity in the opposite direction of the domain and thus the wall velocity is nil relative to a fixed frame of reference (29).

The 'Interface Definition' boundary conditions are fluid-fluid interfaces that can be used to define the sides of the domain as Periodic type boundary conditions. This effectively allows the reduction of the whole annulus model to only one of the 36 identical blade passages. They can also be used to simulate a tip clearance connection, allowing the fluid to pass (29). All the sides were defined as Periodic type boundary conditions, whilst the top surface of the blade was defined as Type: None to simulate the effects of tip clearance.

Figure 22 below helps the reader to understand how the domain boundaries and interfaces were defined.

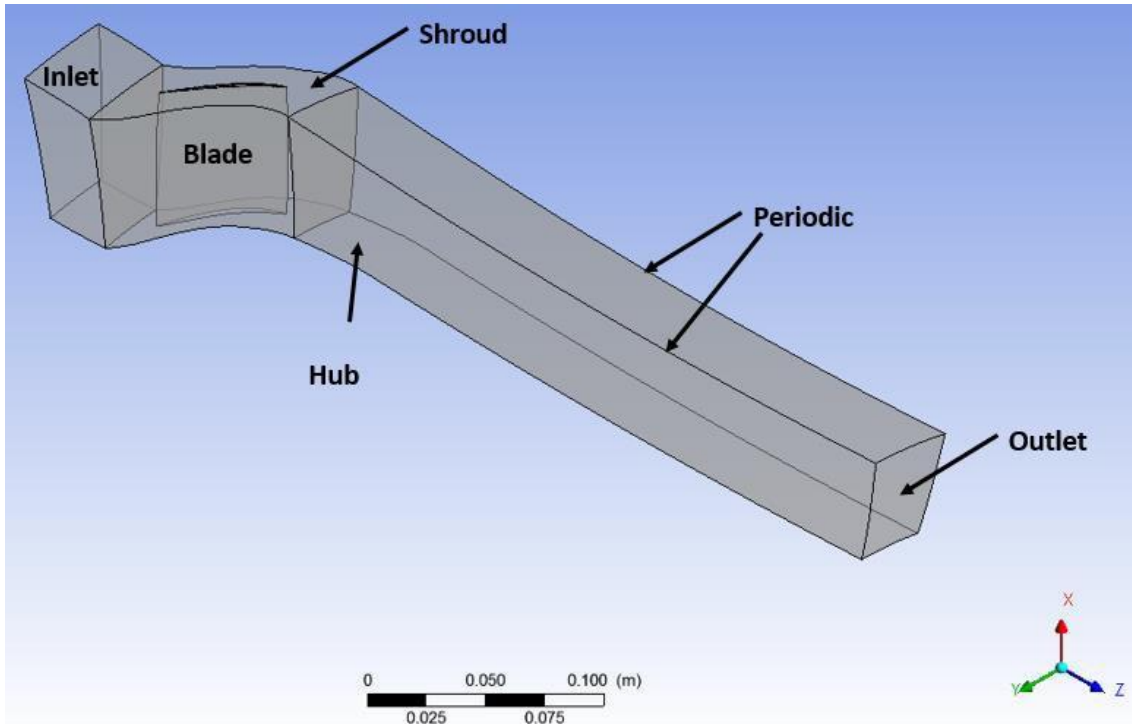


Figure 22: Blade domain definition

4.6 Turbulence model

Turbulence is an extremely complex flow phenomenon which includes a variety of time and space scales. This CFD turbulent flow simulation is carried out as a steady state calculation based on the solution of the RANS equations – a simplified form of the Navier-Stoke equations. These equations simulate only the mean flow quantities whilst the effects of turbulence are modelled by turbulence models (23). The purpose of the current work is to quantify the effects of geometric uncertainty on an axial fan performance when manufacturing anomalies are imposed upon the baseline geometry. It is thus very important, for a realistic simulation, to accurately capture all turbulence phenomena by implementing appropriate turbulence models.

The so-called “two equation eddy-viscosity models” are very popular when it comes to turbulent flow applications. K-epsilon ($k-\epsilon$) is the most notable example of this category. However, this model demonstrates low sensitivity to adverse pressure gradients that induce flow-separating regions, which precludes it from using it in this work.

Wilcox developed the k-omega ($k-\omega$) turbulence model to address the limitations of k- ϵ model. Better transition prediction as well as improved accuracy and solution robustness have been reported using this model. Nevertheless, the model seems to be highly sensible in the region bounded by the free stream velocity and the upper end of the shear

stress layer (29). Based on Wilcox’s model, the Shear Stress Transport or k- ω SST was developed. This model demonstrated lower susceptibility to the adverse pressure gradients assuming a proportional relationship between the turbulent shear stress and the turbulence kinetic energy of a turbulent boundary layer.

According to ERCOFTAC QNET Lucerne Workshop conclusions, no model has been identified with consistently better overall results. However, it is possible that some physical features are predicted better with higher order turbulence models (23). Taking into consideration the above information, k- ω SST was selected as the most appropriate turbulence model to be implemented for the purpose of this study.

4.7 Grid dependency study

Conducting a grid dependency (or convergence) study is considered good practice and should be always a part of any CFD study. This study is undertaken in order to assess the impact of the grid size on the accuracy of the results. It has been already stated that the denser the grid, the more accurate the results. However, in practice a very dense grid results in computational time and resource consuming simulations. It will be shown that above a certain number of elements there is no significant gain in the accuracy of the results and thus a grid that will be considered as the best compromise between computational resources and accuracy will be used for the rest of this study.

A by default fine grid of 250,000 elements was initially chosen and the Compressor Isentropic efficiency and blade Torque were calculated using ANSYS CFX solver. Incrementing the grid size by 250,000 elements per trial, a set of four different simulations (see Table 4) was conducted and the results were plotted against the number of the grid elements.

Table 4: Grid sensitivity study cases

Grid Target	Isentropic	Torque
250000	0.859555	0.802009
500000	0.862165	0.806842
750000	0.865667	0.808342
1000000	0.865872	0.807602

Figure 23 shows that a grid with more than 500,000 elements does not yield significant improvement in the accuracy of the results. Therefore, for the rest of this study this grid will be used.

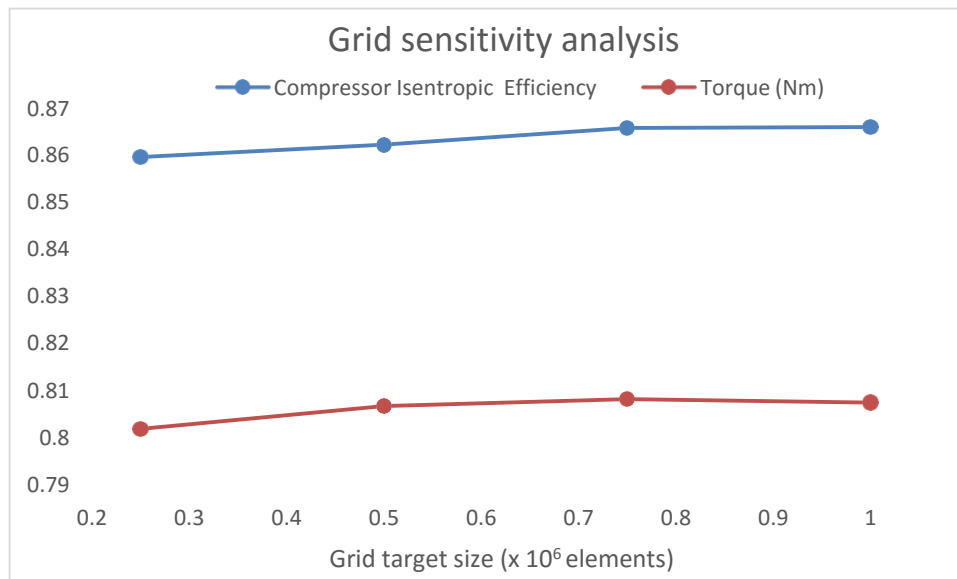


Figure 23: Grid sensitivity analysis

4.8 Monitoring the CFD simulation

Upon the completion of the simulation setup step, a number of CFD simulations were run using ANSYS CFX solver on Cranfield’s PC Lab, four-node, 4GB Ram, parallel processing local computers and Cranfield’s 9 TFlop HPC system.

A good way to check whether a simulation has converged or not, is to monitor the progress of residuals for the equations that are solved iteratively. The residuals represent the magnitude of the calculated error (i.e. the difference) between two subsequent iterations. The equations solved are the Navier-Stokes momentum equations for each direction, the continuity equation (or conservation of mass), equations regarding the turbulence model in use and if heat transfer is applicable, the energy equation. If the residuals are decreasing, it is said that the equation converges to a certain value. This value will be the solution of the problem. On the other hand, if these errors are increasing, the solution is diverging (28). The convergence criteria for this study were set to a residual RMS value of 1E-06. In ANSYS CFX, RMS residual levels of 1E-04 are considered to be loosely converged, levels of 1E-05 are considered to be well converged, and levels of 1E-06 are considered to be tightly converged. Note that it is not always possible to achieve residual levels as low as 1E-06 (30).

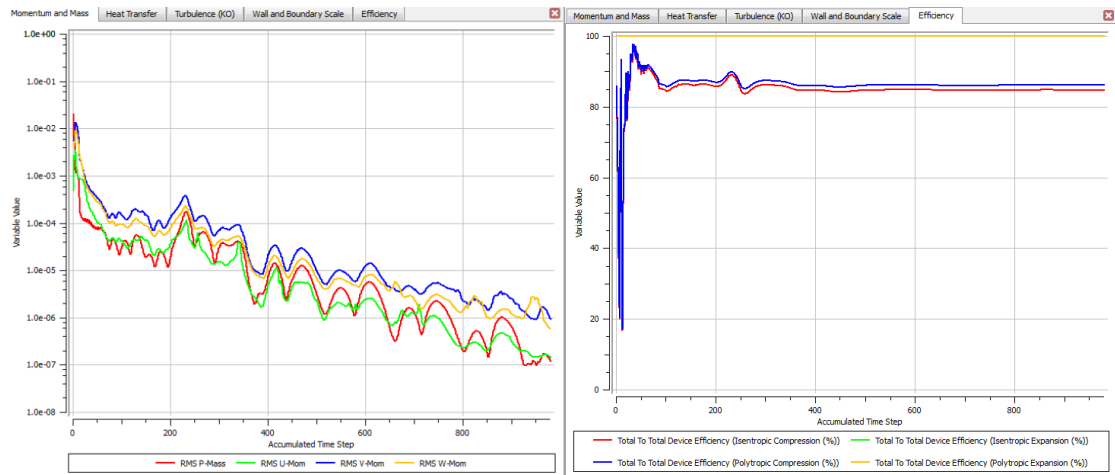


Figure 24: Momentum, Mass and Efficiency residuals of a converging solution

5 CFD results and discussion

Graphical techniques are widely used to obtain an insight into fluid dynamics simulation solution. The results of this CFD study were visualized and analyzed using ANSYS CFD-Post software.

5.1 Baseline geometry

5.1.1 Model Validation

In the last section of the previous chapter it was shown that the solution converged. This does not necessarily imply that the obtained solution is correct. It just signifies that the CFX solver could produce the best possible solution for the given problem. There are a number of factors that determine the accuracy of the solution. E.g. a poor quality or overly coarse mesh or user errors during the setup phase will undoubtedly produce inaccurate results. The results should therefore be compared with reliable data and check if there is an agreement between what was observed in the experiments and the calculated numerical solutions. The much reported transonic Rotor 37 was selected due to the availability of abundant experimental data, including pneumatic probes, thermocouples and LDA measurements. Dozens of papers that report directly or indirectly calculations of this case, have been published (23).

In 1998 AGARD AR-355 published the Rotor 37 experimental results and compared them with thirteen CFD submitted solutions (22). These results will be used to validate the baseline geometry model.

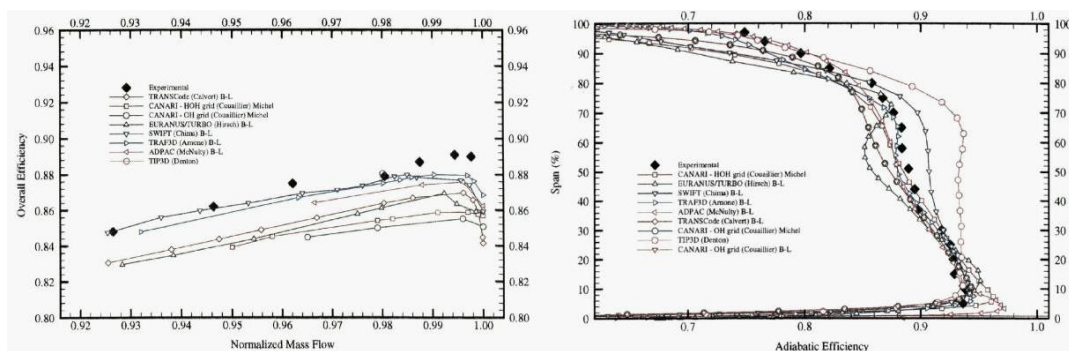


Figure 25: Published Efficiency results of Rotor 37 (22)

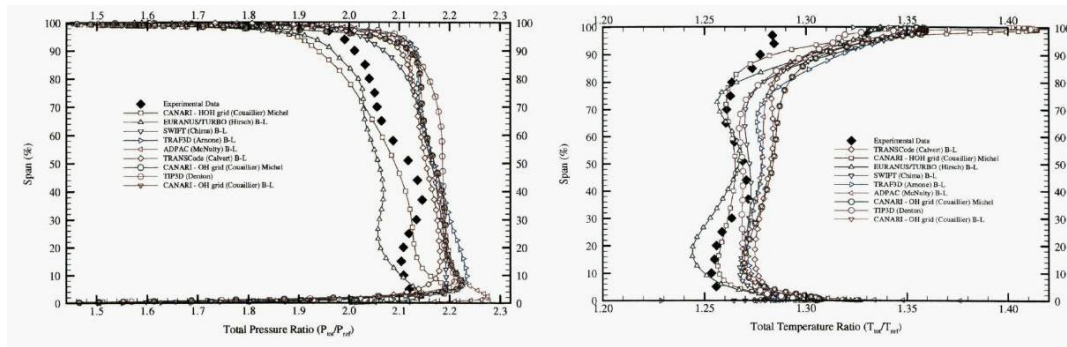


Figure 26: Published PR and TR results of Rotor 37 (Dunham, 1988)

The published data show a large deviation between the CFD submitted results. This can be accredited to a variety of factors. Small geometric and boundary condition differences may significantly alter the simulated results. The choice of the turbulent model also leads to different results. An unexpected source of error may even be the numerical scheme or the implementation of the turbulence model in different CFD codes (23).

Hirsch et al shows that the majority of the submitted FD solutions under-predicted the experimental overall adiabatic efficiency. The radial distribution of the same quantity at Station 4 located at 10.67 cm downstream the blade LE show a 3% under-prediction from 10 to 80% of the blade span. At the top 20% of the blade span almost all simulations predicted a much lower efficiency which implies that most CFD codes over-predict the losses at the tip-wall region (22). Most of the simulations also produce a higher than the experimental pressure and temperature ratio. Deviations from the experimental results may also derive from some form of experimental uncertainty. E.g. some parameters were not measured directly.

The following graphs show the comparison between the experimental results and the simulated ones using the model created for this study. Overall efficiency and pressure and temperature ratios, all show similar trends with the simulated results presented in the AGARD report. An additional source of error may be the fact that in the actual rotor there is a gap upstream of hub and a blade fillet. These geometrical features are not present in the model and may be affecting the results.

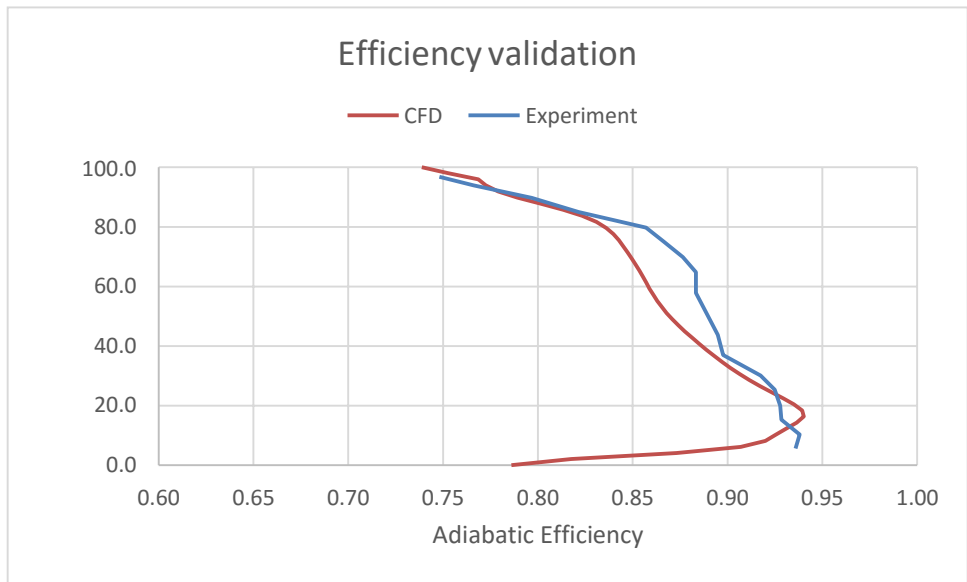


Figure 27: Rotor 37 experimental and computed Efficiency

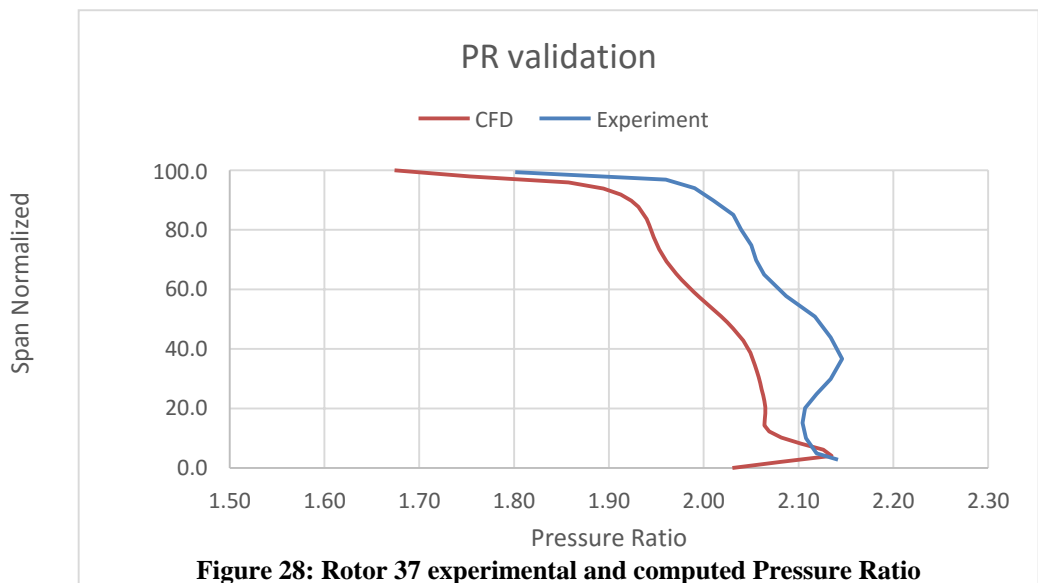


Figure 28: Rotor 37 experimental and computed Pressure Ratio

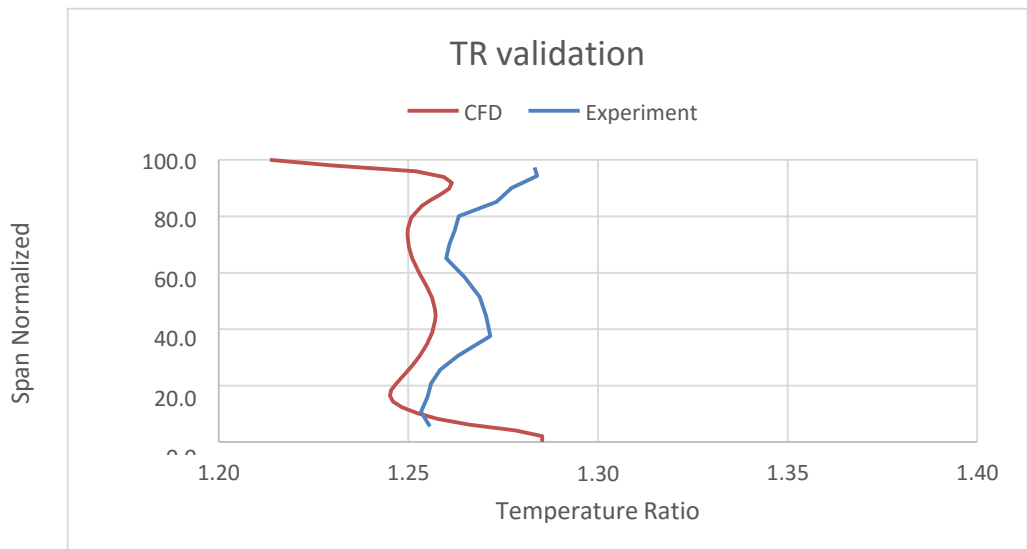


Figure 29: Rotor 37 experimental and computed Temperature ratio

Differences between experimental and simulated results were expected. The reader should have in mind that the aim of this study is to assess the impact of geometric variability on overall compressor performance. This effectively means that CFD tools are used in a comparative way. Any deviation from the experimental data will be transferred to every simulation. What is important is the assessment of the 'deltas' and for that reason the author is confident that the model predicts satisfactory the Rotor 37 flow.

5.1.2 Verification of the mesh clustering

A y plus factor - a measure of the distance between the first cell of the O-Grid and the blade surface - less than one is considered to be a good indicator of a grid that is able to resolve the boundary layer. Figure 41 illustrates the distribution of the y plus along the midspan section. The figure confirms that the mesh is appropriate for low Re calculations. A sharp increase in the y+ value can be observed at the LE of the blade and indicate that there is room for further mesh improvement.

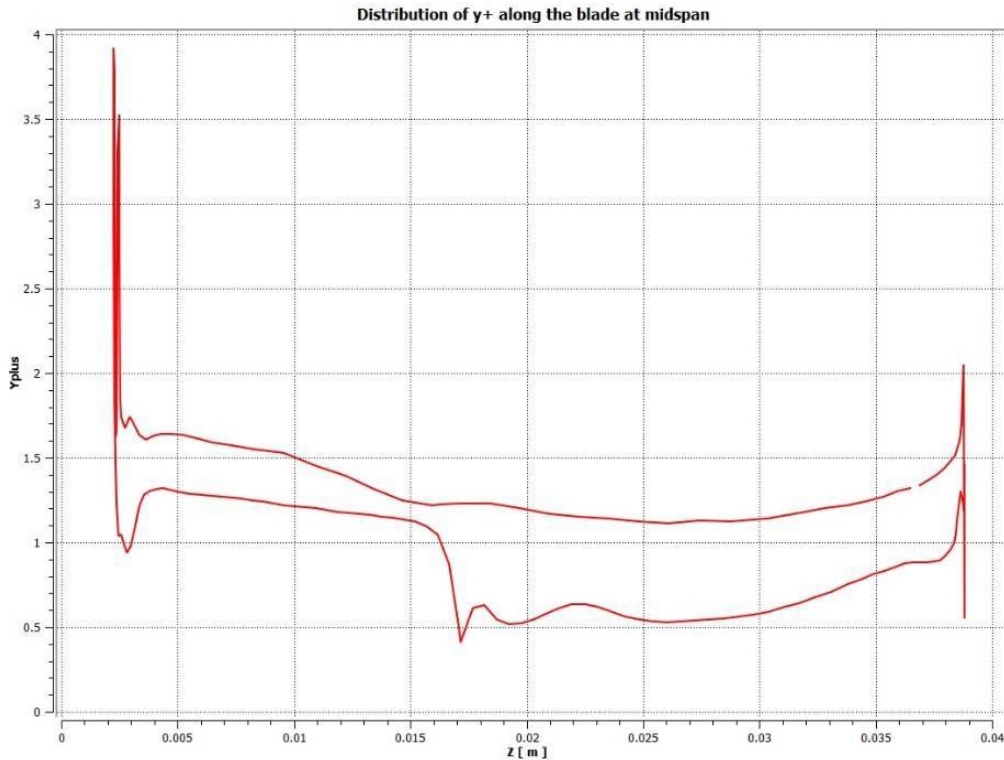


Figure 30: Axial distribution of y^+ along the blade midspan

5.1.3 Rotor 37 characteristic

A set of simulations had to be run in order to explore the choking and stalling limits.

Table 5: Simulation results for different back pressures

Outlet P-Static	Normalized Mass Flow	PR	Overall
99000	0.981248543	1.86001	0.856089
100000	0.981246823	1.86274	0.856297
105000	0.981069661	1.90566	0.860793
110000	0.978812996	1.94642	0.863862
112000	0.976693932	1.96202	0.864539
116000	0.968162637	1.99158	0.863274
118000	0.961533684	2.00465	0.861308
120000	0.953465074	2.01684	0.858711
121000	0.948490779	2.02186	0.856742

To that end the third set of predetermined Inflow/ Outflow Boundary Templates was selected during the set up phase of the simulation (see section 4.5.1). Starting from a low 99 kPa outlet static pressure and increasing till the code cannot produce a converging solution the working line of Rotor 37 is obtained. Figure 31 and Figure 32 show the Pressure Ratio and the Adiabatic Efficiency, plotted against the normalised mass flow respectively and compare them with the experimental values. The normalised mass flow is defined as the calculated mass flow rate over the measured by NASA choke mass flow rate.

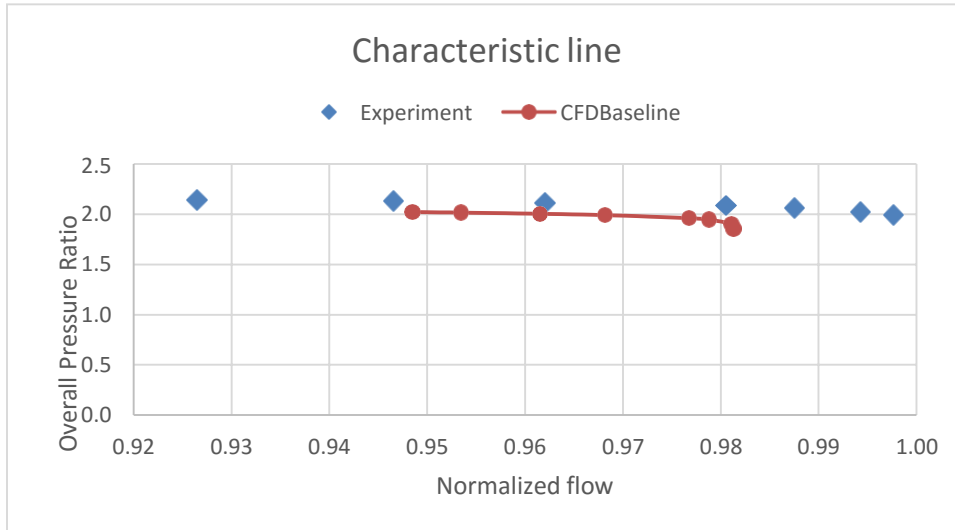


Figure 31: Overall Pressure Ratio against Normalized Mass Flow

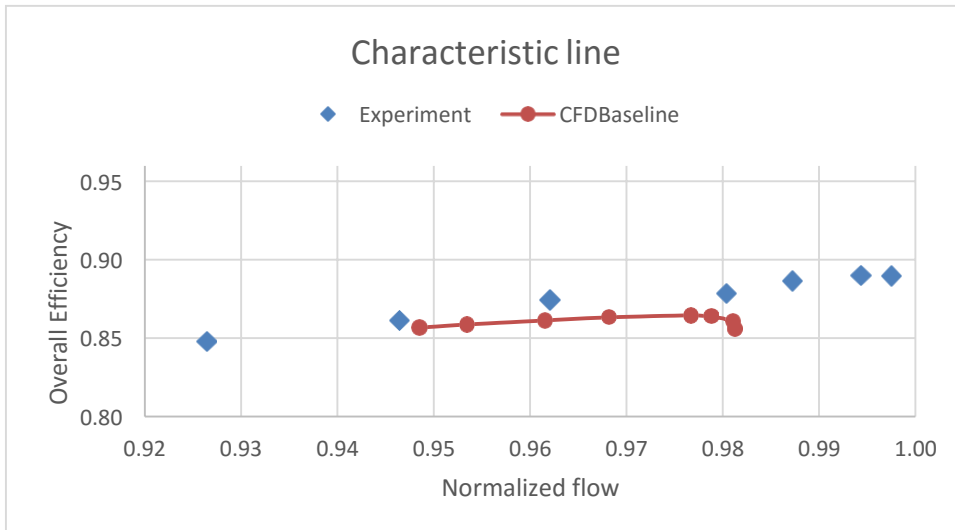


Figure 32: Overall Efficiency over Normalised Mass Flow

A static pressure lower than 99 kPa would not result in an increased mass flow and can be safely stated that this is the choking limit. It can be seen that the code calculates a choke mass almost 2% less than the measured. When asked to solve for back static pressure values higher than 121 kPa the model could not produce a steady state solution and was crashing consistently. It could be assumed that this is when stalling occurs. However, comparison with the experimental results show a noticeable deviation in the back pressure rise that can be achieved.

5.1.4 Flow details

The flow phenomena that occur across the transonic passage are many and complex. In order to understand the flow, a number of blade to blade Mach number contours and blade loading charts at various radii were generated and analysed.

Figures 33-35 show the relative Mach number contours that were generated for the baseline geometry at 5%, 50% and 90% spanwise location respectively. The working fluid flows from left to right and the blades rotate downwards.

There is a single bow shock at all spanwise positions attached to the LE of the blade. The bow shock is a curved shock wave that can be found in a supersonic flow past a finite body and resembles the waves that a ship bow produces as it moves through water. This shock is not necessarily normal to the flow as can be seen in the blade to blade surface and could indicate that the blade could possibly support a slightly greater pressure rise before stalling occurrence (20). The shock interaction with the suction side boundary layer is also visible. Immediately after the LE the flow accelerates rapidly until experiencing a sudden deceleration due to a shock wave. At the hub of the blade there is a shock around 30% of the chord. For the other radii presented in the graphs the shocks are produced slightly downwards and are stronger since higher inlet relative Mach numbers are present. The flow accelerates after the shock for about 25% of the chord and then diffuses as it reaches the TE of the blade. This acceleration and subsequent diffusion could indicate that a separation bubble is formed at the foot of the shock. This separation can be seen more clearly at the higher spans where the flow does not reattach to the blade surface.

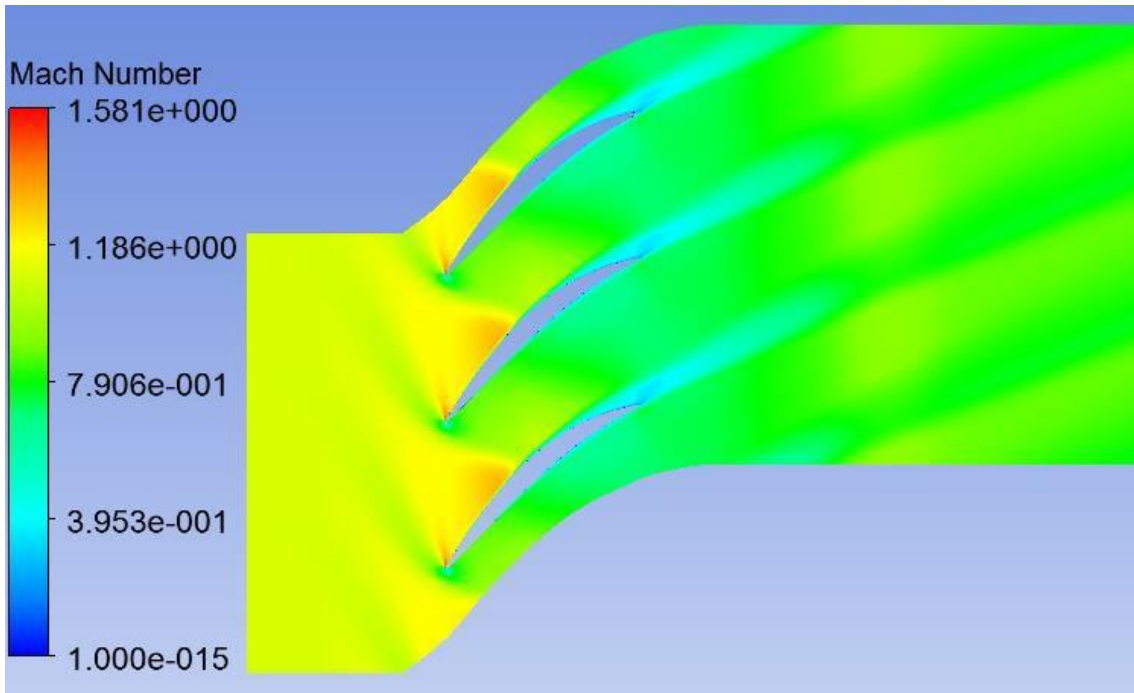


Figure 33: Baseline Mach number contour at 5% span

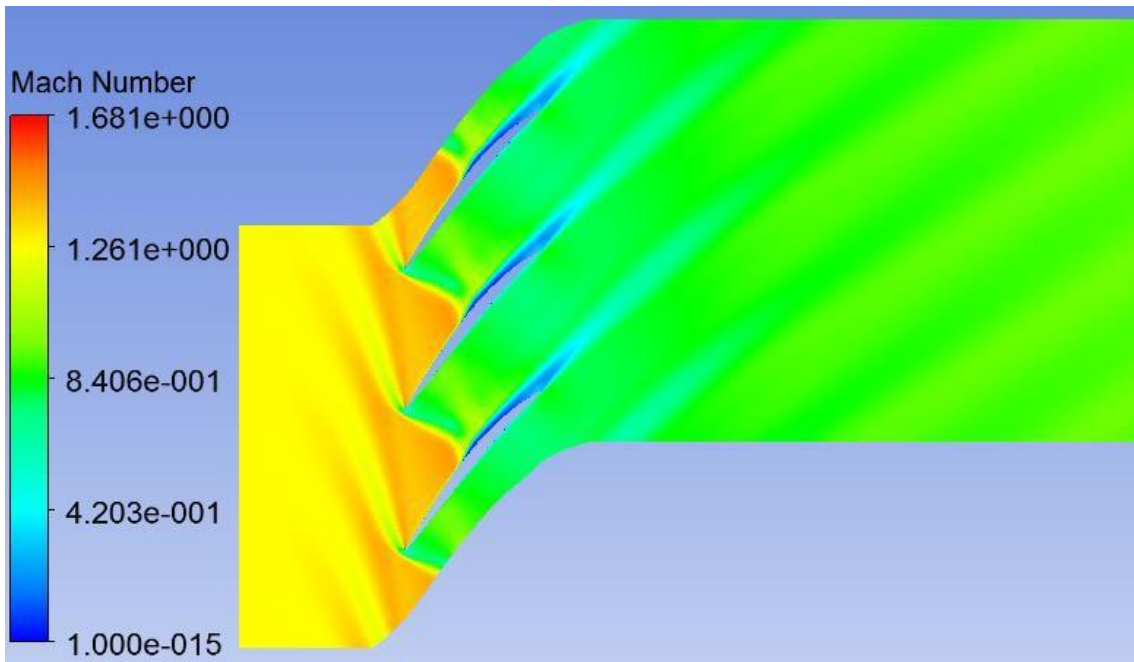


Figure 34: Baseline Mach number contour at 50% span

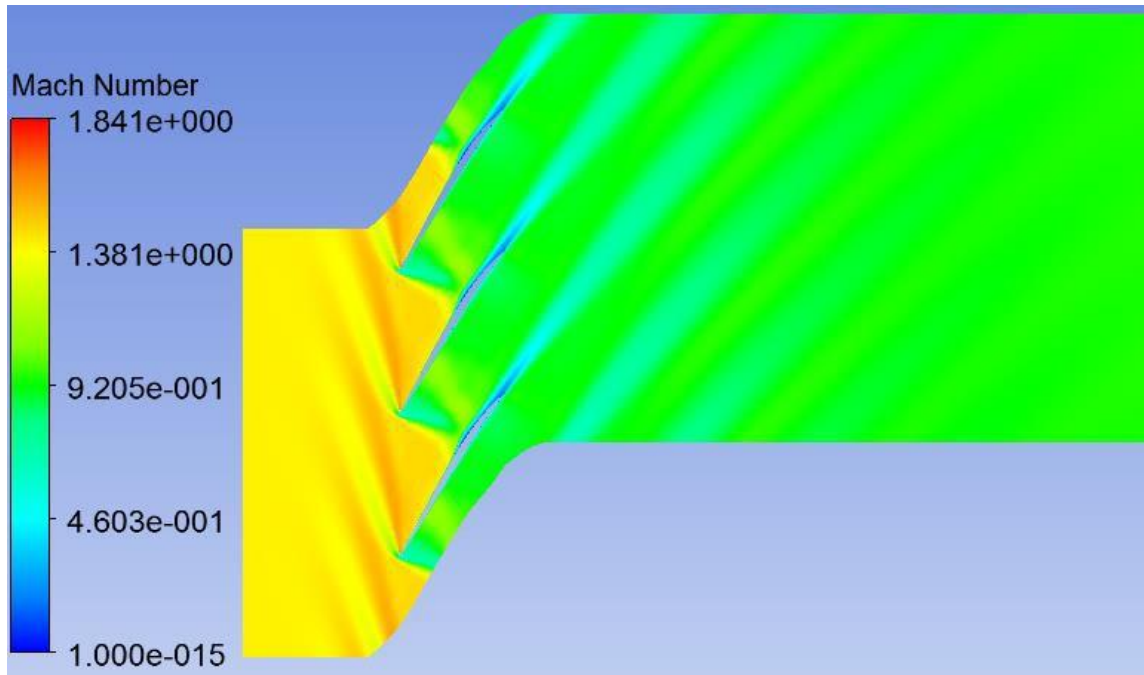


Figure 35: Baseline Mach number contour at 90% span

Figures 36-38 show the blade loading charts generated at the same spanwise locations. The charts plot the static pressure distribution around the blade. Sharp changes in the curve gradient indicate shock waves. The very high pressure values at the LE along the whole span, verify the presence of the aforementioned bow shock wave. In the hub section PS there is a sharp decrease in pressure directly downstream the shock wave which means that the flow accelerates until the 10% of the chord. From this point onwards the flow diffuses until the TE. The SS shows a different pattern. After the bow shock the flow accelerates rapidly to supersonic until 30% of the chord where the flow passes through the second shock wave and then slowly decelerates towards the TE. The pressure distribution around the first half of the suction side should normally vary less. This unusual distribution probably derives from the fact that the fillet of the blade was not modelled and therefore the blade geometry of the rotor near the blade hub is not ideal. Also secondary flows are expected in this area and could explain such behaviour. The pressure distribution charts for the other two sections follow similar patterns.

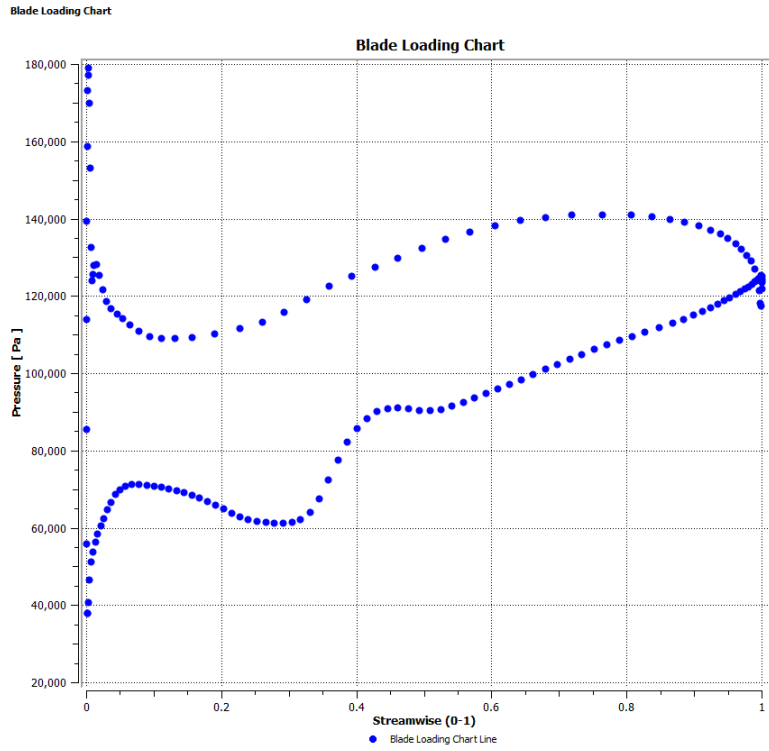


Figure 36: Baseline blade loading chart at 5% span

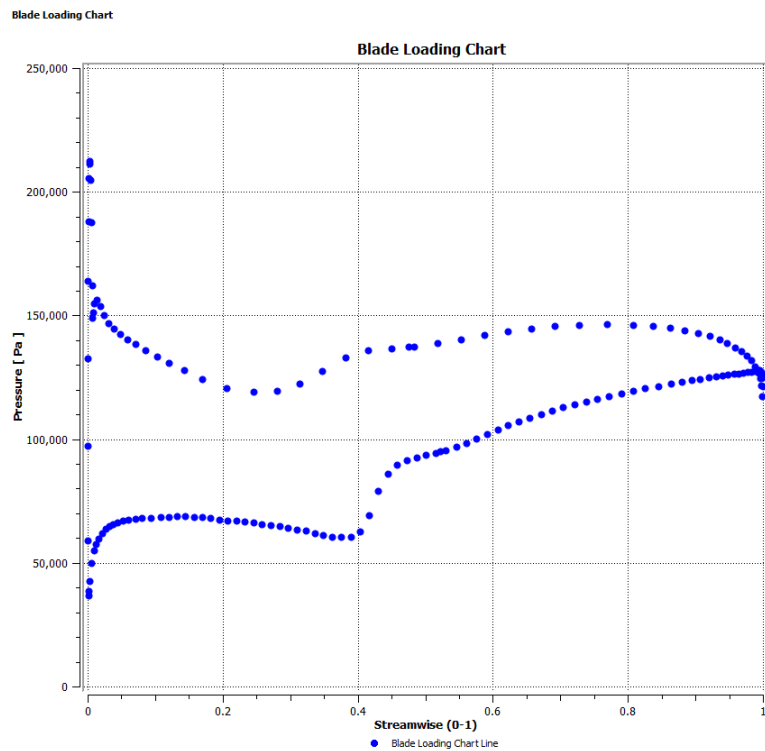


Figure 37: Baseline blade loading chart at 50% span

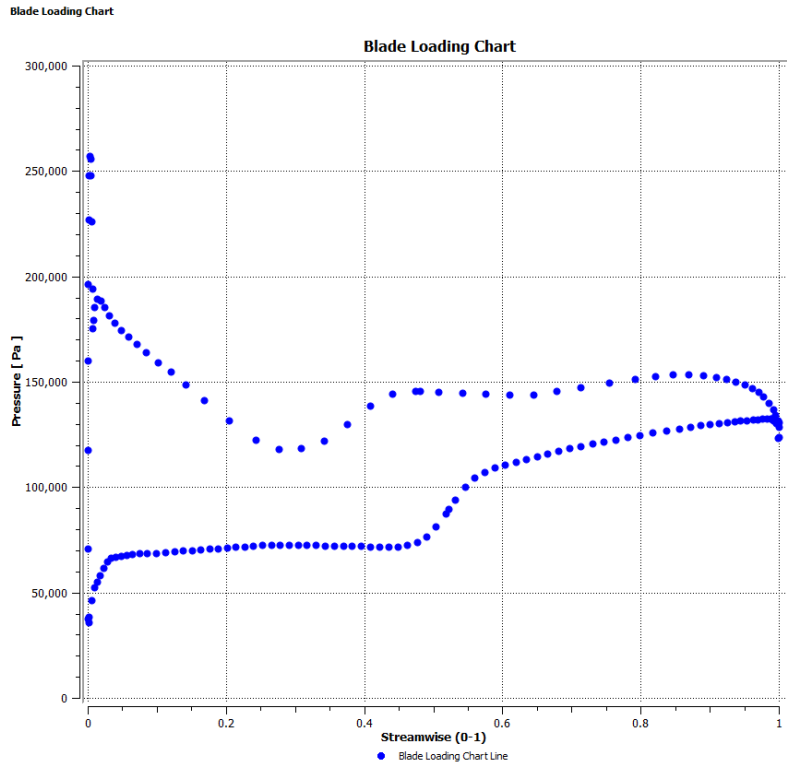


Figure 38: Baseline blade loading chart at 90% span

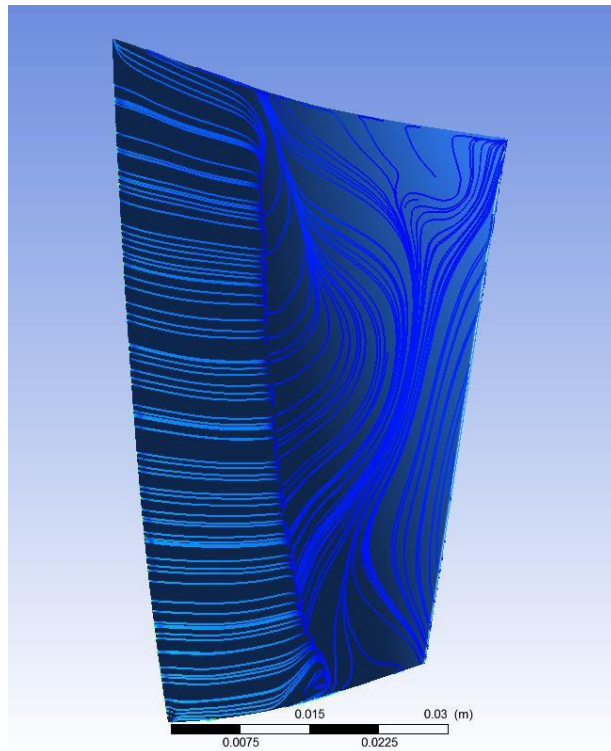


Figure 39: Baseline streamlines on suction side

The streamlines of Figure 39 show a recirculation zone at the hub of the blade that starts at 30% due to interaction of the shock with the boundary layer developed at the suction side. A strong radial migration of streamlines from hub to shroud immediately after the shock wave is predicted. The streamlines travel radially outwards and effectively move high loss fluid from hub to tip and has the effect of increasing the apparent efficiency at the lower half of the blade but decreasing it near the tip.

Figures 40-42 show the distributions of the efficiency, the total pressure and the total temperature along the blade span at Station 4 located 10.67 cm downstream the LE and were analysed in subsection 5.1.1.

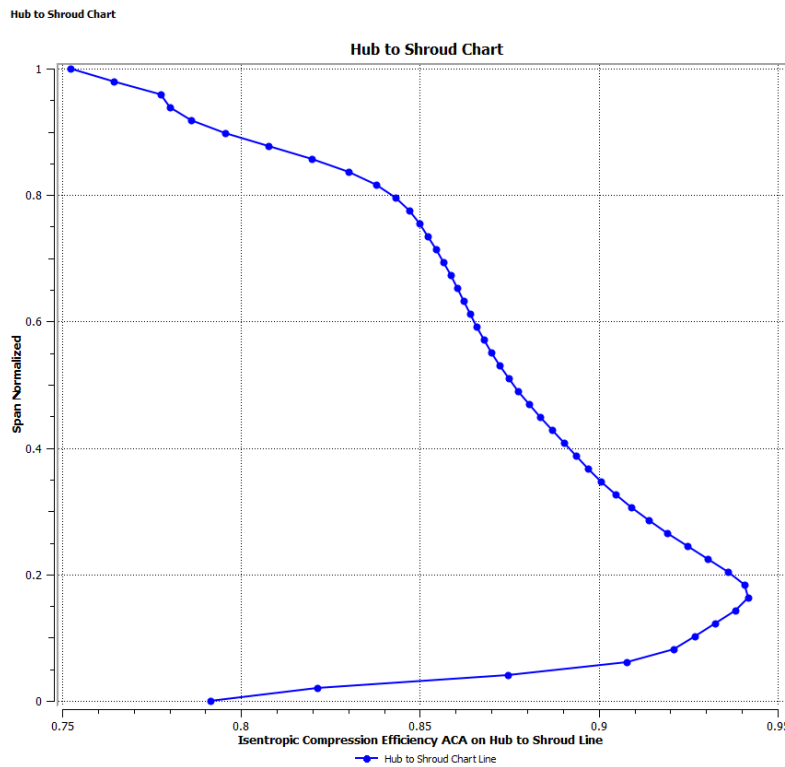


Figure 40: Baseline hub to shroud efficiency distribution

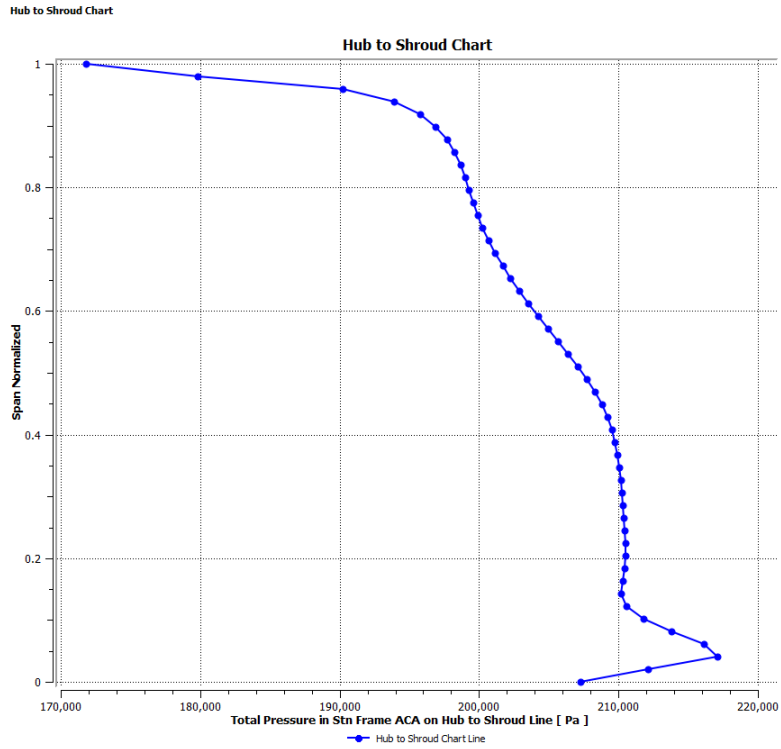


Figure 41: Baseline hub to shroud total pressure distribution

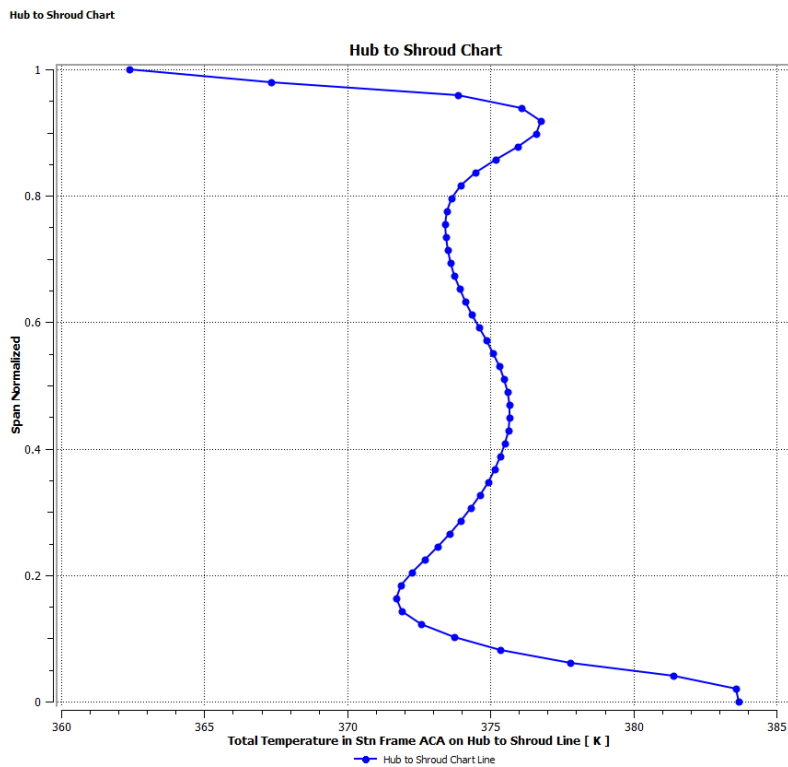


Figure 42: Baseline hub to shroud total temperature distribution

6 CONCLUSIONS AND RECOMMENDATIONS

6.1 Conclusions

The NASA Rotor 37 was used as a baseline geometry for this study. The objective was to study the aerodynamic performance of the blade row. A literature review on the design process of a compressor was undertaken. Then, a high fidelity CFD model of the baseline geometry was successfully created and used to analyse the complex flow phenomena that take place. The computational domain boundaries were kept well away from the blade edges to make allowance for the flow to stabilise and acquire a converging solution. A y^+ factor of 1.22 was achieved which is considered to be a good indicator of the generated grid's ability to resolve the boundary layer. Being an important part of every CFD process, a grid sensitivity study was conducted to find the best compromise between computational resources and the accuracy of the results. The baseline model solutions were validated against experimental results obtained by NASA. A deviation between the solution and the published data was observed and was accredited to a variety of factors. Geometrical features that were not modelled (e.g. gap upstream of hub and blade fillet), boundary condition differences, the choice of the turbulent model and its implementation in the CFD code, even the numerical scheme used by the solver are all considered sources of error. This implies that differences between experimental and simulated results were expected. Since the aim of this study was to assess the impact of geometric variability on overall compressor performance, any deviation from the experimental data is transferred to every simulation and CFD tools are used to assess the 'deltas'. The author deemed that the model predicted satisfactory the Rotor 37 flow and used it in a comparative way. A blunt (squared) and a sharper LE shape modifications were implemented uniformly across the blade span as extreme cases to assess the impact of LE geometric variability on the performance of the component. Comparing the isentropic efficiency distributions, it was observed that from hub till 30% span the efficiency of all geometries is identical. From this span and upwards a gradually increasing gap takes place. In average the predicted efficiency of the squared LE geometry was decreased by 0.94%. The biggest deviation could be found at the tip of the blade where the predicted efficiency declined by 2.35%. The sharper LE overperformed the baseline. In average, the predicted efficiency of the elliptic LE geometry is increased by 0.62%. The CFD model provided useful insights

into the complex Rotor 37 flow phenomena. However, it should be noted once again that CFD do not replace the need for experiments and therefore the simulated results should be validated as were the ones for the baseline geometry. Concluding, a high fidelity model was successfully created and could be used for assessing blade manufacturing uncertainty, thus the objectives of the study were met.

6.2 Recommendations for further work

The geometrical features that are present in the actual Rotor 37 (i.e. gap upstream of the hub, blade fillet) were not modelled and affected the results. A future implementation of such geometric features into the CFD model will increase the accuracy of the simulation and provide more credible results.

The y plus factor distribution around the blade verified that the model was capable to describe, is applied to low Re calculations. However, a sharp increase in the y^+ value was observed at the LE of the blade and indicate that there is room for further mesh improvement locally.

K- ω SST was selected as the most appropriate turbulence model to be implemented for the purpose of this study. However according to ERCOFTAC QNET Lucerne Workshop conclusions, no model has been identified with consistently better overall results. A study comparing the impact of different turbulence models on the results could be undertaken. A comparison between results from different CFD solvers could also be useful.

The study can be developed by studying various shape modifications, in order to assess the effect of manufacturing and design variations and how these affect the performance of the compressor. Some of these can include:

- LE/TE shape variations
- Tip clearance deviations
- Creation of a step/bumps across the blade
- Airfoil leaning: axial or tangential
- Airfoil twist (deviations in stagger)
- Deviations from actual measurements of airfoil stacking (some A/F sections seems to deviate in a consistent way)

Also, an overall study should include the effect that the performance of one -or even more- component has on the overall gas turbine performance. Using the CFD results, further work can take place with the use of zero-dimensional tools that have the capability to assess the overall performance of a gas turbine.

REFERENCES

1. *Impact of geometric variability on axial compressor performance*. Garzon, Victor E and Darmofal, David L. Atlanta, Georgia, USA : Proceedings of ASME Turbo Expo 2003, Power for Land, Sea, and Air, 2003. GT2003-38130.
2. Garzon, Viktor. *Probabilistic Aerothermal Design of Compressor Airfoils*. Massachusetts: Massachusetts Institute of Technology, 2003.
3. Saravanamuttoo, Herb, et al *Gas Turbine Theory 6th Edition*. Essex, England: Pearson Education Limited, 2009.
4. Hall, Nancy. National Aeronautics and Space Administration Glenn Research Center. *Compressors*. [Online] 05 May 2015. <http://www.grc.nasa.gov/WWW/K-12/airplane/compress.html>.
5. Zachos, Pavlos. *Turbomachinery Course Notes Axial Compressor Design and Performance Slides*. Cranfield : Cranfield University, 2014.
6. Boyce, Meherwan P. National Energy Technology Laboratory. *Axial-Flow Compressors*. [Online] 17 August 2013. <http://www.netl.doe.gov/File%20Library/Research/Coal/energy%20systems/turbines/handbook/2-0.pdf>.
7. Ramsden, K W and Zachos, Pavlos. *Turbomachinery Course Notes - Compressors*. Cranfield : Cranfield University, 2014.
8. Bentley, David. *Aerodynamic fan design for a high bypass turbofan engine with 1.4 pressure ratio*. Cranfield : Cranfield University, 2013.
9. Kopanakis, Georgios. *Design and CFD analysis of a fan with an inverted pressure profile for noise reduction*. Cranfield : Cranfield University, 2013.
10. Rowlands, David O. *Core compressor aerodynamic design*. Cranfield : Cranfield University, 2013.

11. Mc Bride, Mark W. *The design and analysis of turbomachinery in an incompressible, steady flow using the stramline curvature method*. Washington : The Pennsylvania State University Applied Research Laboratory, 1979.
12. Gallimore, S J. *Axial flow compressor design*. Derby : Rolls-Royce plc, 1999.
13. Mehrotra, Prateek. *Aerodynamic design and CFD assessment of a highly loaded, high efficiency transonic fanfor a turbofan engine*. Cranfield : Cranfiel University, 2013.
14. Aungier, Ronald H. *Axial flow compressors : A strategy for aerodynamic design and analysis* . New York : ASME Press and Professional Engineering Publishing, 2003.
15. Royce, Rolls. Rolls-Royce. *Defence Aerospace; EJ200*. [Online] 28 July 2015. <http://www.rolls-royce.com/customers/defence-aerospace/products/combat-jets/ej200.aspx#engine-specifications>.
16. Jackson, Paul. *Jane's All the world's aircraft: development and production: 2015-2016*. New York : McGraw-Hill, 2015.
17. Latham, Annelise N. *Design modification for the EJ200 Turbofan to enhance Typhoon supercruise capability*. Cranfield : Cranfield University, 2011.
18. Pachidis, Vassilios A. and Nikolaidis, Theoklis. *Gas Turbine Performance Simulation*. Cranfield : Cranfield University, 1999.
19. Schobeiri, Meinhard T. *Turbomachinery Flow Physics and Dynamic Performance*. Berlin : Springer Berlin Heidelberg, 2012.
20. Escauriaza, Mariana. *Effects of manufacturing tolerances on Gas Turbine performance and components*. Cranfield : Cranfield University, 2015.
21. *Lessons from Rotor 37*. Denton, J D. 1996, Journal of Thermal Science, pp. Vol.6, No.1.
22. Hirsch, C and Tartinville, B. *Rotor 37*. s.l. : NUMECA.

23. Dunham, J. *AGARD Advisory Report 355 - CFD Validation for Propulsion System Components*. Neuilly-Sur-Seine : AGARD, 1988.
24. Teixeira, Joao Amaral. *Computational Fluid Dynamics Vol. 2*. Cranfield : Cranfield University, 2014.
25. Montomoli, Francesco, et al. *Uncertainty Quantification in Computational Fluid Dynamics and Aircraft Engines*. s.l. : Springer International Publishing AG Switzerland, 2015.
26. Tu, Jiyuan. *Computational Fluid Dynamics: A Practical Approach*. s.l. : Butterworth Heinemann, 2007.
27. Rubini, Phi. *Computational Fluid Dynamics Vol. 1*. Cranfield : Cranfield University, 2014.
28. *Ansys R15.0 Help files*. 2015.
29. CFD Online. *Dimensionless wall distance (y plus)*. [Online] 28 March 2014. [http://www.cfd-online.com/Wiki/Dimensionless_wall_distance_\(y_plus\)](http://www.cfd-online.com/Wiki/Dimensionless_wall_distance_(y_plus)).
30. Mariuta, Alexandru Cristian. *Fan modelling a twindmilling and locked rotor conditions*. Cranfield : Cranfield University, 2013.
31. Kuron , Michael. CAE Associates. *Has My CFD Analysis Converged? - Part I*. [Online] 22 August 2014. <https://caesai.com/blog/has-my-cfd-analysis-converged-par>